Monthly Notices of the ROYAL ASTRONOMICAL SOCIETY

MNRAS **531,** 510–529 (2024) https://doi.org/10.1093/mnras/stae1165
Advance Access publication 2024 May 6

Dark Energy Survey Year 6 results: Intra-cluster light from redshift 0.2 to 0.5

Yuanyuan Zhang [1,2★] Jesse B. Golden-Marx [3] Ricardo L. C. Ogando [4] Brian Yanny,[5] Eli S. Rykoff,[6,7] Sahar Allam,[5] M. Aguena,[8] D. Bacon [9] S. Bocquet,[10] D. Brooks,[11] A. Carnero Rosell,[8,12,13] J. Carretero,[14] T.-Y. Cheng,[15] C. Conselice,[16,17] M. Costanzi,[18,19,20] L. N. da Costa,[8] M. E. S. Pereira,[21] T. M. Davis,[22] S. Desai,[23] H. T. Diehl,[5] P. Doel,[11] I. Ferrero,[24] B. Flaugher,[5] J. Frieman,[5,25] D. Gruen,[10] R. A. Gruendl,[26,27] S. R. Hinton,[22] D. L. Hollowood,[28] K. Honscheid,[29,30] D. J. James,[31] T. Jeltema,[28] K. Kuehn,[32,33] N. Kuropatkin,[5] O. Lahav,[11] S. Lee,[34] M. Lima,[35,8] J. Mena-Fernández,[36] R. Miquel,[14,37] A. Palmese,[38] A. Pieres,[8,4] A. A. Plazas Malagón,[6,7] A. K. Romer,[39] E. Sanchez,[36] M. Smith,[40] E. Suchyta,[41] G. Tarle,[42] C. To,[29] D. L. Tucker,[5] and N. Weaverdyck[42,43] (DES Collaboration)

Affiliations are listed at the end of the paper

Accepted 2024 April 24. Received 2024 April 23; in original form 2023 August 27

ABSTRACT

Using the full 6 years of imaging data from the Dark Energy Survey, we study the surface brightness profiles of galaxy cluster central galaxies and intra-cluster light. We apply a 'stacking' method to over 4000 galaxy clusters identified by the redMaPPer cluster finder in the redshift range of 0.2−0.5. This yields high-signal-to-noise circularly averaged profile measurements of the central galaxy and intra-cluster light out to 1 Mpc from the cluster centre. Using redMaPPer richness as a cluster mass indicator, we find that the brightness of the intra-cluster light has a strong mass dependence throughout the 0.2−0.5 redshift range, and this dependence grows stronger at a larger radius. In terms of redshift evolution, we find some evidence that the central galaxy, as well as the diffuse light within the transition region between the cluster central galaxy and intra-cluster light within 80 kpc from the centre, may be growing over time. At larger radii, more than 80 kpc away from the cluster centre, we do not detect evidence of additional redshift evolution beyond the cluster mass dependence, consistent with the findings from the IllustrisTNG hydrodynamic simulation. We speculate that the major driver of intra-cluster light growth, especially at large radii, is associated with cluster mass growth. Finally, we find that the colour of the cluster central galaxy and intra-cluster light displays a radial gradient that becomes bluer at a larger radius, which is consistent with a stellar stripping and disruption origin of intra-cluster light as suggested by simulation studies.

Key words: galaxies: evolution - galaxies: clusters: general.

1 INTRODUCTION

Galaxy clusters contain a diffuse stellar component of intra-cluster light (ICL). First discovered more than half a century ago (Zwicky 1951, 1952), ICL is abundant around the cluster central galaxies (CGs) or the brightest cluster galaxies (BCGs) and contains stars dispersed into the intra-cluster space. It has been studied using optical or infrared imaging and spectroscopic observations, which have been reviewed in Abraham et al. (2017), DeMaio (2017), Contini (2021), Arnaboldi & Gerhard (2022), and Montes (2022). Because of the ICL's faint brightness and the overall difficulties of studying low surface brightness (SB) features (Abraham et al. 2017; Mihos 2019), ICL has remained a poorly understood subject until recently, when the number of studies jumped with refreshed interests due to new data (Montes & Trujillo 2022), simulations (Shin et al. 2022), and techniques (Marini et al. 2022).

Simulation and semi-analytical studies have investigated ICL formation in many different channels (e.g. Rudick, Mihos & McBride 2006; Sommer-Larsen 2006; Barai, Brito & Martel 2009; Rudick et al. 2009; Puchwein et al. 2010; Martel, Barai & Brito 2012; Contini et al. 2014) including galaxy disruption, stellar stripping, merging (Murante et al. 2004, 2007; Contini, Yi & Kang 2018), and pre-processing (Chun et al. 2022). The ICL's formation is often studied together with the evolution of cluster CGs or even the cluster's overall galaxy distribution due to difficulties in separating the two (e.g. Monaco et al. 2006; Conroy, Wechsler & Kravtsov 2007; Cooper et al. 2015; Pillepich et al. 2018; Cañas et al. 2020). Different channels of ICL formation carry implications for the ICL's observational properties and their redshift evolution in terms of age,

★ E-mail: yuanyuanzhang.astro@gmail.com

colour, and metallicity (Harris et al. 2017; Contini, Yi & Kang 2019), fraction of ICL in the cluster stellar light (Murante et al. 2007; Purcell, Bullock & Zentner 2007; Cui et al. 2014; Tang et al. 2018), morphology (Rudick et al. 2006), or scaling relation to cluster mass or mass distribution (Alonso Asensio et al. 2020; Contini & Gu 2021). For example, Contini et al. (2019) analysed ICL colour and metallicity using semi-analytical models, which contain ICL formed through tidal stripping of cluster satellite galaxies as well as through merging relaxation; they found a negative radial colour and metallicity gradient. From hydrodynamic simulations, Pillepich et al. (2018) found that ICL stellar mass strongly correlates with the host halo mass, but this correlation appears to evolve little from redshift 1 to 0.

In observational studies, the formation and evolution of ICL has been studied using its colour (e.g. Mackie 1992; Krick, Bernstein & Pimbblet 2006; Montes & Trujillo 2014; DeMaio et al. 2015), stellar mass (Krick et al. 2011; Burke et al. 2012; DeMaio et al. 2020; Spavone et al. 2020; Barfety et al. 2022), stellar population spectroscopic studies (e.g. Coccato, Gerhard & Arnaboldi 2010a; Coccato et al. 2010b, 2011; Ventimiglia, Arnaboldi & Gerhard 2011; Arnaboldi et al. 2012; Longobardi, Arnaboldi & Gerhard 2015a; Barbosa et al. 2016; Edwards et al. 2016) and is often investigated together with BCG evolution (e.g. Gonzalez, Zabludoff & Zaritsky 2005; Zhang et al. 2016; Golden-Marx et al. 2022). For example, DeMaio et al. (2020) studied the stellar mass of BCG and ICL between redshift 0.05 and 1.75 and found its growth rate to be greater than that of the cluster by a factor of 2. They also found that the core of the BCG formed early while the BCG outskirt and ICL were built at later times. On the other hand, detailed analysis of local BCG and ICL stellar populations by Edwards et al. (2020) indicate that while the stellar population in the ICL is old, it is still younger (≈9 Gyr) than the BCG (≈13 Gyr), pointing towards a late and continuous formation of ICL through minor merging.

In this work, we continue the observational study of ICL evolution by examining its properties in the redshift range of 0.2−0.5. Our work is based on thousands of galaxy clusters and the full 6 years of observations from the Dark Energy Survey (DES; Abbott et al. 2021), a wide-field imaging survey (DES Collaboration 2005) designed to probe cosmic structures in the late Universe (e.g. Abbott et al. 2020; DES Collaboration et al. 2022; Abbott et al. 2022a, b). We use a 'stacking' method (Zibetti, White & Brinkmann 2004; Zibetti et al. 2005; Tal & van Dokkum 2011; Zhang et al. 2019c; Sampaio-Santos et al. 2021; Chen et al. 2022; Ahad, Bahé & Hoekstra 2023) with the DES galaxy cluster sample to reduce measurement noise. Our goal is to acquire high-signal-to-noise measurements of the ICL SB profile, colour, and luminosity and quantify their evolution between redshift 0.2 and 0.5. This paper presents one of the largest ICL redshift evolution studies based on a cluster sample a few times larger than that in Golden-Marx et al. (2023a), who used a cluster sample from the Atacama Cosmology Telescope based on cosmic microwave background observations.

One challenge to ICL studies is the difficulty in disentangling ICL from cluster CGs (see discussions in Dolag, Murante & Borgani 2010; Contini, Chen & Gu 2022). Although stars in the intra-cluster space may have different stellar composition or dispersion dynamics (e.g. Longobardi et al. 2015b; Hilker et al. 2018; Longobardi et al. 2018a, b; Gu et al. 2020; Pérez-Hernández et al. 2022) than cluster CGs or BCGs − from imaging data alone, it is often difficult to separate the ICL from the low-SB outskirts of those galaxies. Different separation methods have been suggested (Rudick et al. 2011), including analytical decomposition, using a machine learning algorithm (Marini et al. 2022), SB limits (Presotto et al. 2014), or using physical distance apertures to separate those components. In this paper, we follow the practice of Pillepich et al. (2018) who analysed CG and ICL as the 'diffuse light' of galaxy clusters. We use the phrase diffuse light interchangeably with CG+ICL in this paper. When needed, we use a physical aperture to separate CG and ICL, with ICL defined as the diffuse light beyond 30 kpc from the CG centre (an outer radius limit is defined according to the context), while CG is defined as the diffuse light component within 30 kpc.

The remainder of this paper is organized as the following. In Section 2, we review our data sets and the methods. Section 3 presents our measurements of the diffuse light SB, while Section 4 quantifies the cluster mass and redshift dependence of the diffuse light luminosities. Section 5 discusses observational effects that may impact the interpretation of our results, and Section 6 discusses our results in the context of simulations and other observational studies. Section 7 summarizes our findings. Throughout this paper, we assume a flat ΛCDM cosmology with $\Omega_m = 0.3$ and $h = 0.70$.

2 DATA AND METHODS

2.1 The REDMAPPER galaxy cluster catalogue

The red sequence Matched-filter Probabilistic Percolation cluster finder algorithm (REDMAPPER; Rykoff et al. 2014) has been used by the DES Collaboration to derive galaxy cluster catalogues from the Science Verification data, (Rykoff et al. 2016), the Year 1 observations (McClintock et al. 2019), and the Year 1−3 observations (O'Donnell et al. 2021). REDMAPPER is a red-sequence based algorithm that provides excellent cluster richness (λ) and photometric redshift estimates (Rykoff et al. 2014). It also provides a random point catalogue that tracks the sky footprint and depth covered by the cluster-finding algorithm.

This paper is based on the REDMAPPER cluster catalogue, version 6.4.22+2, derived from the DES Year 3 Gold data sets (Sevilla-Noarbe et al. 2021). A relevant difference between this catalogue and the DES Year 1 version (McClintock et al. 2019) is the much larger sky coverage. As a result, this catalogue contains more than 21 000 galaxy clusters with richness above 20, which approximately corresponds to a halo mass threshold of $10^{14.1}$ $M_\odot$ (Farahi et al. 2019; McClintock et al. 2019). These galaxy clusters are detected from the DES single-object fit (SOF) catalogue (Drlica-Wagner et al. 2018; Sevilla-Noarbe et al. 2021), which contains objects detected and deblended by SOURCE EXTRACTOR (Bertin & Arnouts 1996), while the photometry was derived from single-object fitting using the `ngmix` algorithm on multi-epoch image stamps of each object, and the deblended nearby objects are masked on each single-epoch image. For the DES Year 3 data-processing campaign, the SOF photometry measurements are preferred in many applications because of the tighter photometry constraints compared to the SOURCE EXTRACTOR measurements derived using the coadded images.

Of particular importance to this analysis, REDMAPPER provides CG candidates for each cluster. Unlike algorithms that aim to select the BCGs, REDMAPPER aims to select a relatively luminous cluster galaxy that is nearest to the cluster's gravitational centre, and the goal of this selection is to find the CG of the massive dark matter halo as defined in simulation modelling studies (e.g. De Lucia & Blaizot 2007; Yang, Mo & van den Bosch 2008). REDMAPPER provides five CG candidates for each cluster, and we use the most likely CG candidate. Multi-wavelength studies have shown that this candidate is the correct one with an ∼ 80 per cent frequency (Saro et al. 2015; Zhang et al. 2019a; Bleem et al. 2020), and we further

Table 1. The galaxy cluster sample in this analysis.

Redshift (z) Bin	Richness (λ) Bin	Number counts	Median z	Mean z	Median λ	Mean λ	R_λ (Mpc/h) Based on mean λ	Masking limit (z −band) `mag_auto`
0.2–0.3		1169	0.256	0.255	28.55	33.61		20.67
	20–30	656	0.254	0.253	23.72	24.17	1.03	
	30–45	326	0.259	0.256	35.51	35.97	1.23	
	45–60	121	0.257	0.255	50.51	51.16	1.44	
	60+	66	0.274	0.263	73.55	83.58	1.80	
0.3–0.4		1556	0.359	0.355	27.33	32.92		21.38
	20–30	942	0.359	0.354	23.70	24.11	1.03	
	30–45	399	0.358	0.355	35.44	36.01	1.23	
	45–60	115	0.360	0.356	52.56	52.06	1.45	
	60+	100	0.361	0.355	75.25	81.57	1.78	
0.4–0.5		1357	0.449	0.449	27.13	32.10		21.87
	20–30	836	0.449	0.449	23.44	23.97	1.03	
	30–45	349	0.451	0.449	35.14	35.90	1.23	
	45–60	96	0.454	0.452	51.08	51.78	1.45	
	60+	76	0.440	0.445	69.83	79.17	1.76	

discuss the effect of mis-centring on interpreting our measurements in Section 5.4.

In addition, we make use of the REDMAPPER richness quantity as a cluster mass indicator. This richness quantity is a probabilistic number count of the red sequence member galaxies (Rykoff et al. 2012) in a cluster and analyses with weak lensing (Melchior et al. 2017; Murata et al. 2018; McClintock et al. 2019), X-ray (Mantz et al. 2016), and CMB (Saro et al. 2015) observations have placed quantitative constraints on the scaling relation between REDMAPPER richness and cluster mass. Because richness scales excellently with cluster mass, and the scaling relation does not appear to change with redshift (McClintock et al. 2019), we qualitatively interpret richness dependence of CG and ICL observational features as cluster mass dependence, but quantitative analysis in the future can be carried out using analytical relations between richness and cluster mass.

For this diffuse light analysis, we apply a few additional selection criteria to the REDMAPPER clusters as well as to the REDMAPPER random points. (1) Around the cluster centre (or a random point), in a circular region with a radius of 0.15 deg, we require at least one DES exposure image in each of the g, r, i, and z filters. (2) Around the cluster centre (or a random point), in a circular region with a radius of 0.15 deg, we require the 10σ depth magnitude of the DES AUTO measurements to be deeper than a redshift-dependent 'masking' magnitude (see next section for details). This selection criterion ensures that our diffuse light measurements are comparable between different redshift slices. The cut has minimal effect on the clusters/randoms below redshift 0.4 but excludes a small fraction of the clusters between redshift 0.4 and 0.5 and most of the clusters above redshift 0.5. (3) Around the cluster centre (or the random point), in a circular region with a radius of 0.2 deg, we exclude areas containing famous or bright stars (the Yale bright stars or 2MASS stars of $J < 8$).[1], nearby galaxies including the Large Magellanic Cloud, and globular clusters to reduce scattered light in the images.

After applying these selection criteria, we are left with a sample of over 4000 clusters in the redshift range of 0.2−0.5. The number of clusters in each richness/redshift bin is listed in Table 1. We also include clusters in the redshift range of 0.5−0.6 in some of the analyses in this paper. However, because of the DES depth limit, we are concerned that our galaxy masking procedure (see Section 2.3) may be incomplete in this redshift range[2] and above. Therefore, the measurements of the 0.5−0.6 clusters are presented only for illustrative purposes and are not included in our quantification of diffuse light evolution.

We note that a redMaPPer galaxy cluster catalogue based on the full six years of DES observations is also internally available to the DES collaboration. However, we opt to use the Year 3 version described here because its richness definition has better consistency with the Year 1 version in McClintock et al. (2019), which provides the richness-mass relation used in our estimations. The redMaPPer catalogue based on Year-s 1−6 observations goes to higher redshift ($z \sim 0.9$) than the Year 3 version in this paper (which is based on Years 1−3 observations), but both versions have excellent redshift coverage in the 0.2−0.5 redshift range studied in this paper.

2.2 DES object catalogues and images

In this paper, we use the DES images and catalogues produced by the Dark Energy Survey Data Management (DESDM) project (Sevilla et al. 2011; Morganson et al. 2018). A detailed description of the DESDM pipeline can be found in Abbott et al. (2018). To summarize, the DESDM pipeline takes raw images from the Dark Energy Camera (DECam) (Flaugher et al. 2015), performs instrumental signature removals and corrections (Plazas, Bernstein & Sheldon 2014; Gruen et al. 2015), flat-field corrections (Bernstein et al. 2018), full-focal-plane background subtractions (Bernstein et al. 2017b), as well as photometric (Burke et al. 2018) and astrometric (Bernstein et al. 2017a) calibrations to produce science-ready single exposure images.

[1]This cut requires HEALPix values in the DES foreground map file to be less than 2.

[2]The redshift 0.5−0.6 clusters will be masked to 22.32 mag in z-band in `mag_auto`. Only ~ 1 per cent of the redMaPPer clusters reach 22.3 mag in the DES 10σ z-band depth map continuously in the whole 0.15 deg^2 region around them and a depth-based cut would eliminate most of the clusters. For comparison, The redshift 0.4−0.5 clusters will be masked to 21.9 mag in z-band in `mag_auto`, while 67 per cent of the redMaPPer clusters reach 21.9 mag in the DES 10σ z-band depth map continuously in the whole 0.15 deg^2 region around them. Note that the DES coadd catalogues are generally over 95 per cent complete above 23.7 mag in z-band, and the decision of a depth cut is made out of an abundance of caution.

Those images are coadded (Bertin et al. 2002) into multi-epoch coadd images, which are used to produce object catalogues and photometry measurements by the SOURCE EXTRACTOR software (Bertin & Arnouts 1996). The science-ready single exposure images are also used as input for photometry measurements such as the NGMIX photometry measurements mentioned in the previous section.

For this work, we benefit from the full 6 years of DES operations (Diehl et al. 2018), and the DES Data Release 2 (DR2) processing campaign (Abbott et al. 2021) which includes not only more data, but also improved processing since the previous data release. Changes and improvements relevant to our analysis include: coadded images based on single-epoch full-focal-plane background subtraction, which do not include local background subtraction as applied to previous versions of DES coadd images (we use the '_nobkg' version of the coadd images, which do not have the local short-scale sky background subtracted as mentioned in Section 2.3); combining DES *r*-, *i*- and *z*-band images into detection images as an average to create more robust faint objects detection; finally, changing the source detection threshold from 10σ to 5σ to produce more complete object catalogues. The DR2 coadd images have a combined sky coverage of 4913 deg^2 in DES *g*, *r*, *i*, *z*, and *Y* bands, and the 95 per cent completeness of the coadd catalogues reaches 23.7 magnitude in the DES *z*-band, with a 10 σ magnitude limit of 23.1.

We use both DES images and catalogus in this paper. Other than the REDMAPPER cluster catalog, the coadd object catalogues used in this paper are constructed from DES coadd images using the SOURCE EXTRACTOR software to detect and deblend objects. Moreover, we make use of the object's AUTO measurements from SOURCE EXTRACTOR to determine each object's masking area, which is based on Kron apertures and magnitudes (Kron 1980). The images used in this paper include both the science-ready single exposure images and the multi-epoch coadd images. In the next section, we describe how we use these images and catalogues in our workflow.

2.3 The averaging/stacking method

In this paper, we again use a 'stacking' method described in Zhang et al. (2019c), which has also been adopted in Leung et al. (2020); Sampaio-Santos et al. (2021); Golden-Marx et al. (2023a). We present ICL and CG properties averaged over a large cluster sample. The 'stacking' method proceeds as the following:

(i) Coadd images of each galaxy cluster, are downloaded from the DESDM data base[3] For each image, we mask all objects above a *z*-band magnitude limit determined by the cluster's redshift. We exclude the REDMAPPER CG from masking to preserve the CG light. The masking magnitude is chosen to be $0.2L*$ with $L*$ being the characteristic luminosity of a cluster red galaxy luminosity function measurement (Zhang et al. 2019b). Assuming a faint end slope of -1, this masking limit would remove 82 per cent of the light from cluster galaxies.

(ii) After masking, the radial SB profile is derived from the masked images, as the mean pixel value in circular radial annuli on the images. Thus, the derived profiles are the circularly averaged profiles for each cluster. Note that Brough et al. (2024) compared ICL fraction measurements using both circular and elliptical apertures and did not find significant impact.

(iii) Similarly, radial SB profiles are derived for a sample of random points that cover the same sky area as the cluster catalogue. In later steps, those random profiles are subtracted from the cluster profiles to eliminate residual backgrounds in the cluster profiles.

(iv) Using a Jackknife resampling method (see examples of applications in Norberg et al. 2009; Melchior et al. 2017), we divide the cluster samples, and the random points into 40 subsamples according to their sky coordinates.[4] For each sky coordinate subsample, we derive the CG+ICL SB profile by averaging the profiles of clusters and randoms in circular apertures, and then subtracting the random profiles from that of the clusters. We then apply the Jackknife resampling method (Efron 1982) to those sky coordinate subsamples to derive the means and uncertainties of the final CG+ICL measurements.

(v) Additional quantities, such as the CG+ICL colour and luminosities are further computed from the circularly averaged SB profiles of CG+ICL. In this paper, we also analyse the SB profiles of the cluster total light including CG, ICL, and cluster satellite galaxies. Those measurements are derived using the same procedures listed here, but without the objects masking described in step (i).

We highlight one difference between this paper and Zhang et al. (2019c), Leung et al. (2020), Sampaio-Santos et al. (2021), and Golden-Marx et al. (2023a). In Step (i), for each cluster, the previous analyses processed and coadded single exposure images from DESDM. For this work, we make use of the already coadded images from the DESDM data base. Those DESDM images are based on the single exposure images, but coadded without applying local background subtraction steps in the SWARP and SOURCE EXTRACTOR software. In Section 5.3, we compare the profiles derived from those coadded images and those based on the single exposure images Zhang et al. (2019c); Leung et al. (2020); Sampaio-Santos et al. (2021); Golden-Marx et al. (2023a). The results are highly consistent.

The computational resources needed for this method are not trivial. The masking of a 0.15×0.15 deg^2 region centred on one galaxy cluster, depending on the masking magnitude, can take a few minutes to hours with a single CPU processor. For this work, the masking and profile measurements of each cluster/random point is performed on the Open Science Grid,[5] a High Throughput Computing Consortium. The processing of tens of thousands of clusters or random locations is distributed to thousands of parallel processes on the Open Science Grid in an 'opportunistic' mode. Given the need to test and validate the analyses with different set-ups, we estimate that up to hundreds of thousands of CPU hours have been used in this work.

3 ICL SURFACE BRIGHTNESS

3.1 Richness and redshift dependence

Our first analysis is the circularly averaged SB radial profiles of the diffuse light (CG+ICL), as well as the SB of the total cluster stellar content including the rest of the cluster galaxies. The goal of this analysis is to visually examine the shapes of those profiles and their general redshift/richness trends. The galaxy clusters are split into redshift and richness sub-samples, and those SB profiles are presented in Fig. 1.

We use three redshift bins from 0.2 to 0.5 to analyse the clusters. In each redshift bin, the clusters are further divided into four richness bins, with the richness binning defined in previous DES cluster-lensing studies (McClintock et al. 2019) and listed in Table 1. As mentioned in Section 2, we apply the 'stacking' procedure to each

[3] https://des.ncsa.illinois.edu/desaccess/

[4] https://github.com/esheldon/kmeans_radec

[5] https://opensciencegrid.org

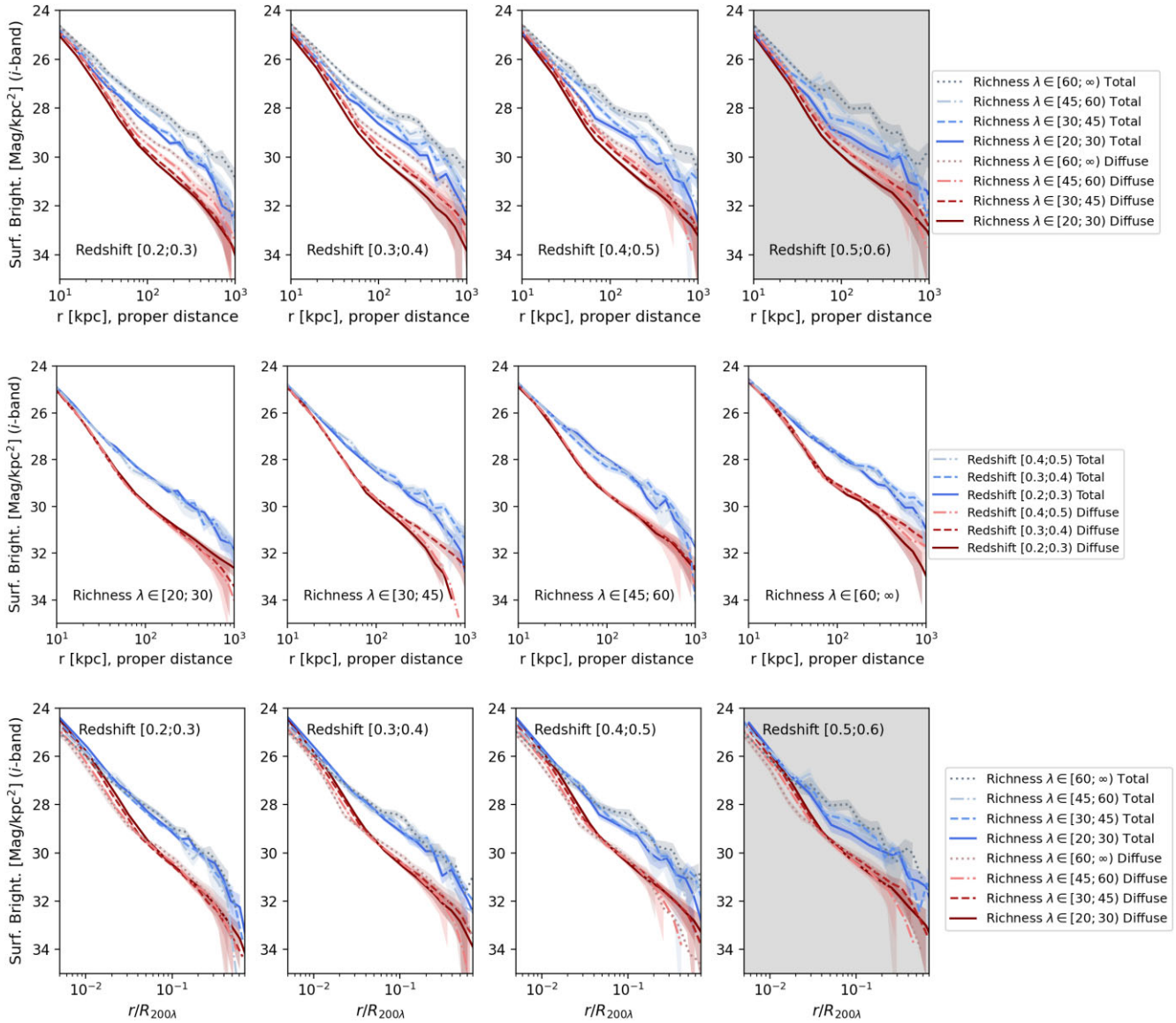

Figure 1. SB of the clusters in richness/redshift ranges. Upper row: Clusters in the same redshift ranges in each panel, with different lines representing different richness subsamples. We show both the SB of the diffuse light (CG+ICL, red hues) and also the SB of total cluster light (blue hues). Both profiles display strong richness dependence across the four redshift panels. Middle row: Clusters in the same richness ranges in each panel, with different lines representing different redshift subsamples. Again, we show both the SB of the diffuse light (CG+ICL, red hues) and also the SB of total cluster light (blue hues). We do not observe consistent redshift trends across the richness panels, indicating weak, if any, signs of redshift evolution. We quantify the significance of the redshift/richness trends in the next Section. Lower Row: SB profiles after the cluster's radius has been scaled by a percolation radius (corresponding to the cluster subsample's average R_{200m}). The radial profiles of the diffuse light as well as the clusters' total stellar contents are 'self-similar' after radial scaling.

redshift/richness binned cluster subsample. The residual background for each subsample is derived from random points, but the masking magnitude limit for the random points is adjusted according to the cluster subsample's redshift range. For each redshift bin, we apply luminosity distance corrections and account for angular distance changes so that the measurements are shifted to be in the observer frame of redshift 0.25. Note that we do not apply a K-correction or evolutionary correction to these measurements. Between redshift 0.45 and 0.25, the combination of these two corrections can change between approximately −0.04 and 0.03 magnitude assuming different stellar population models (using simple stellar population Bruzual & Charlot 2003 models with initial mass functions from Salpeter 1955; Chabrier 2003, metallicity values of 0.008, 0.02, 0.5 and formation redshift between 2 and 10). In addition, the correction is often significantly smaller than the value/uncertainty of the redshift evolution constraints we will later show in Table 2 ($b \times \log_{10}\frac{1.45}{1.25}$). Thus, we present the measurements without applying the evolutionary and K-corrections.

Fig. 1 presents our SB measurements. In each of those richness and redshift bins, we measure the diffuse light profiles up to 1 Mpc from the centre. Our measurements agree with previous studies which show the radial extension of ICL up to several hundreds of kpc, or even one Mpc from the cluster centre (Zibetti et al. 2005; Krick & Bernstein 2007; Kluge et al. 2021; Chen et al. 2022; Li et al. 2022).

Table 2. constraints on parameters in $L(R_0 < r < R_1) = a \times \log_{10}\frac{\lambda_0}{20} + b \times \log_{10}\frac{1+z_0}{1.25} + c$, which is used to quantify the relation between stellar luminosity and cluster richness and redshift.

	a	b	c
$r \leq 30$ kpc Total	-0.73 ± 0.05	2.23 ± 0.34	17.593 ± 0.014
$r \leq 30$ kpc Diffuse	-0.79 ± 0.07	1.76 ± 0.46	17.764 ± 0.019
30 to 80 kpc Total	-1.37 ± 0.09	-0.32 ± 0.80	17.75 ± 0.027
30 to 80 kpc Diffuse	-1.28 ± 0.09	-0.01 ± 0.55	18.68 ± 0.023
80 to 300 kpc Total	-1.76 ± 0.12	-0.66 ± 1.02	16.315 ± 0.036
80 to 300 kpc Diffuse	-1.76 ± 0.12	-0.10 ± 1.11	17.699 ± 0.039
300 to 600 kpc Total	-1.78 ± 0.21	-1.53 ± 1.97	16.117 ± 0.070
300 to 600 kpc Diffuse	-2.00 ± 0.31	-1.39 ± 3.04	17.578 ± 0.105

The upper panels of Fig. 1 show the (circularly-averaged) SB profiles of the galaxy clusters first split by redshift and then by richness. In each subpanel, the redshift range of the clusters is fixed to be the same and each line represents a different richness range. Those radial SB profiles show a clear richness dependence: richer galaxy clusters generally are brighter in SB, while less rich clusters are fainter. The trends are observed for both the diffuse light, and for the total light including cluster satellite galaxies. Moreover, the distinctions between the different richness subsamples are present throughout the three redshift bins, indicating robust richness dependence across the 0.2–0.5 redshift range. Our result supports previous findings that detect strong ICL correlations with cluster mass (e.g. Gonzalez et al. 2005; Montes & Trujillo 2019; Huang et al. 2020; Kluge et al. 2021; Sampaio-Santos et al. 2021; Chen et al. 2022; Huang et al. 2022; Ragusa et al. 2022; Golden-Marx et al. 2023a). Further, the SB richness dependence in Fig. 1 grows more prominent with enlarging radius.

In the middle panel of Fig. 1, we present the SB profiles, first split by richness and then by redshift. In each subpanel, the richness range of the clusters is fixed to be the same and each line represents a different redshift range. Interestingly, those redshift-divided profiles appear similar within their uncertainty ranges; while fixing the cluster's richness range, we do not observe a consistent trend of the SB profiles being either brighter or fainter at a lower redshift. The lack of a consistent trend does not necessarily indicate that there is no redshift evolution for a richness-fixed sample, but potentially an evolution that is too small to be noticeable in those SB figures. In Section 4, we further quantify the redshift-related trends using their luminosity measurements.

3.2 ICL 'Self-Similarity'

Previously we have noted the remarkable similarity of the ICL SB profiles after scaling by the cluster's radius in Zhang et al. (2019c); Sampaio-Santos et al. (2021). Similarly, in this analysis, we investigate this effect with a much larger sample.

Given the relatively small richness range of each bin, we use a similar procedure as described in Sampaio-Santos et al. (2021) to scale the radial profiles. For each richness bin, we rescale the clusters' SB profiles by one radius determined by the average richness of each richness bin. Because there are no weak-lensing mass measurements for the galaxy cluster samples studied in this paper, we scale their radial SB profiles by the redMapper percolation radius which is a function of richness, $R_{200\lambda} = 1.95 \times (\lambda/100)^{0.45}$Mpc h^{-1}. This radius relation is based on the $R_{200\mathrm{m}}$ to richness relation derived using the DES Year 1 richness–mass relation (McClintock et al. 2019), and meant to be an approximation of $R_{200\mathrm{m}}$ derived from cluster richness. We note that the richnesses are not necessarily consistent between different versions of the redMaPPer catalogues based on different DES data releases (a small difference has been found in preliminary comparisons). The percolation radii used here is a close but not necessarily accurate estimation of the clusters average R_{200m}.

The last row of Fig. 1 shows the SB radial profiles after scaling by the percolation radius. This row is meant to be compared to the top row of the same figure (without radial rescaling). These scaled profiles, both of the diffuse light and the cluster light, indeed appear to be much more similar across the richness bins, especially outside a transition radial range around 0.04 $R_{200\lambda}$. In the central regions, the profiles do not appear to be similar after rescaling, suggesting that the CG SB profiles can not be well described by scaled cluster radii. This phenomenon can be explained by an inside-out growth scenario (Oser et al. 2010; van Dokkum et al. 2010), such that CG stellar cores formed early at $z > 2$, while the accretion of CG outskirts and the ICL profiles happen later and are more influenced by the galaxy cluster's mass accretion process.

3.3 Volume-limited cluster sample

In the previous section, we have shown that when fixing the cluster's richness, clusters in different redshift ranges have similar SB profiles. However, this does not answer the question of how ICL and CGs evolve with time in a single galaxy cluster whose richness will also evolve with time – more likely, their richnesses/masses will increase over time because of ongoing merging events.

In this section, we account for cluster richness evolution by constructing a volume-limited cluster sample in different redshift bins. Specifically, in the highest redshift bin of 0.4–0.5, we compute the cosmic volume contained in this redshift bin, and select the clusters above richness of 50. For the lower redshift bins, 0.3–0.4 and 0.2–0.3, we again compute their respective cosmic volumes, and then adjust the richness thresholds for the cluster selections, so that each redshift subsamples have the same cluster density given their different cosmic volumes. For the redshift slice of 0.3–0.4, the richness threshold becomes 55 and for the redshift slice of 0.2–0.3, the richness threshold becomes 61. Only clusters above those richness thresholds are selected for comparison in this section. These selections ensure that the cluster samples have the same spatial densities in each redshift bin. A similar volume-limited selection method is also use in Golden-Marx et al. (2023a), with the distinction that Golden-Marx et al. (2023a) select clusters based on SZ-computed masses, while this analysis is using optical richness.

The SB-profiles of those volume-limited samples are presented in Fig. 2. We again do not observe significant differences between the redshift sub-samples, as the previous section has already noted no visible differences between redshift subsamples within fixed richness ranges. In this exercise, we limit the analysis to a high richness threshold which tends to have lower richness-to-mass scatter (Farahi et al. 2019; Anbajagane et al. 2020) and is less subjective to potential systematic effects such as line-of-sight projections (Costanzi et al. 2019; Abbott et al. 2020; Wetzell et al. 2022; Wu et al. 2022). For the same reason, we also do not sub-divide the clusters according to richness. The consequently smaller sample size lowers the significance of a possible redshift trend. We further quantify the redshift-related trend in Section 4.

3.4 Colour radial profiles

We derive the $r - i$ colour of the circularly-averaged ICL radial profiles using measurements of the DES r and i band SB profiles.

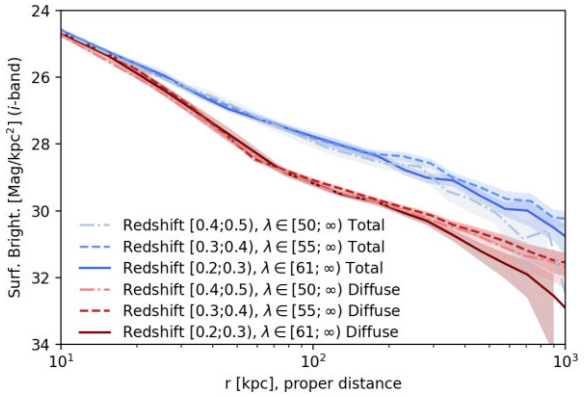

Figure 2. SB of a volume-limited cluster sample. The radial profiles of these redshift subsamples appear to be consistent within the measurement uncertainties, indicating a redshift evolution that is below a detection level. Again, we show both the SB of the diffuse light (CG+ICL, red hues) and the total cluster light (blue hues). We will further quantify the redshift evolution of the cluster luminosities in the next section.

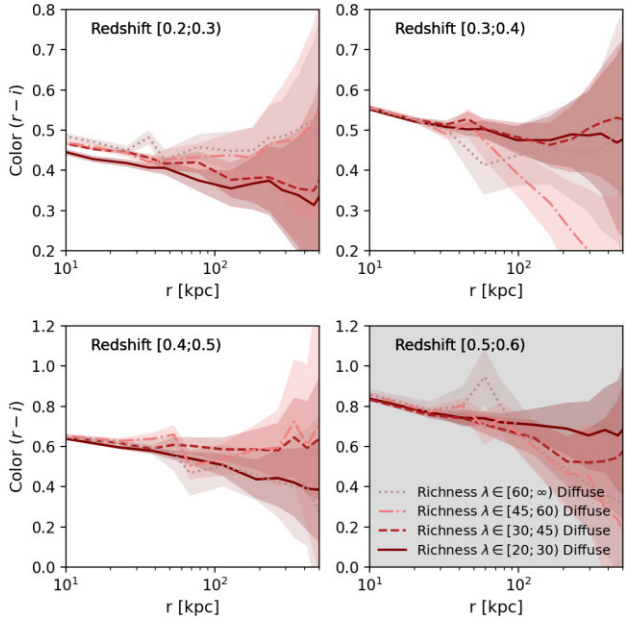

Figure 3. The DES $r - i$ colour profile of the diffuse light in cluster subsamples of different redshift and richness ranges. The diffuse light color is consistent with the average colour of the cluster's total stellar content in the centre. In addition, a radial gradient can be seen in all of the redshift and richness ranges, such that the diffuse light becomes bluer at larger radii. This is consistent with previous studies that ICL consists of more metal-poor and younger stars (Edwards et al. 2020) and suggests an ICL origin from galaxy disruption and tidal stripping (Contini et al. 2019).

These colour measurements are shown in Fig. 3. Given that such measurements require highly significant ICL SB profiles in two bands, we only show colour measurements out to a radius slightly beyond 400 kpc.

The colour profiles are presented in redshift subpanels with clusters further divided in richness bins. As previously noted in the literature, the colour of the diffuse light displays a radial gradient, becoming bluer at a larger radius. Interestingly, we also notice a consistent, although not significant, richness trend in those colours,

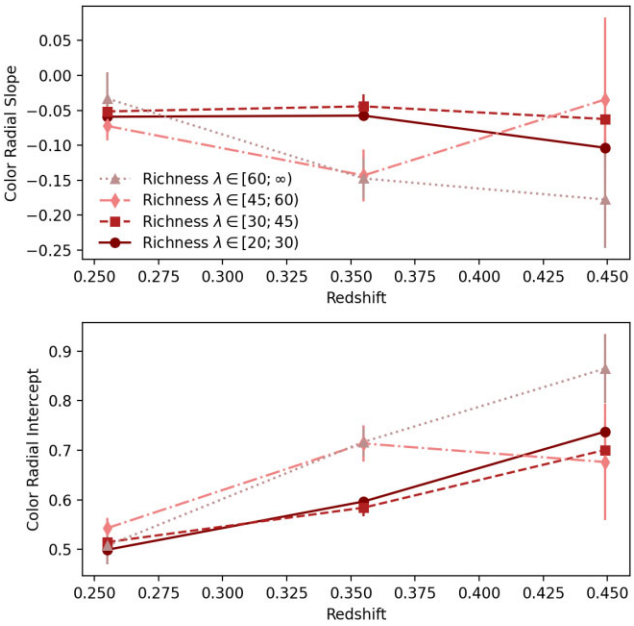

Figure 4. We fit the colour profiles in Fig. 3 to a linear model with radius $\text{Color}(R) = a \times log(R) + b$ to further quantify those profiles. The radial slope parameter a (upper panel) is negative for all of the richness and redshift bins, which is a robust detection of the radial gradient of the diffuse light's colour profile. The b parameter (lower panel), which is the diffuse light's color at $R = 1$ kpc, appears to be slightly larger for richer clusters, possibly reflecting a more massive and redder satellite population in richer clusters.

which appear to be redder in richer clusters. In addition to the diffuse light colour profiles, we have acquired the colour measurements of the cluster's total stellar content, but the measurements are much more uncertain because of Poissonian noise. However, we note that the average colour of the cluster's total stellar content is generally consistent with the colour of the diffuse light.

To further quantify the colours, we fit those measurements as a function of radius:

$$\text{Color}(R) = a \times \log(R) + b \quad (1)$$

Here, a is the radial slope of the colors, and b is the intercept of the profile at $R = 1.0$ kpc. The fitted parameters are shown in Fig. 4. In each redshift/richness bin, a appears to be negative, indicating a robust detection of a radial gradient. This is consistent with previous measurements of ICL radial color gradient (e,g., Zibetti et al. 2005; DeMaio et al. 2018; Yoo et al. 2021; Chen et al. 2022) and that the ICL consists of more metal-poor and younger stars (e.g. Edwards et al. 2020) compared to the CG. As mentioned and analyzed in Contini et al. (2019), the colour radial gradient suggests that the ICL's origin is from galaxy disruption and stripping: if clusters acquire ICL mainly through merging, ICL would have a relatively uniform colour because of stellar population mixing. On the other hand, the disruption and stripping of cluster satellite galaxies would produce a radial gradient because of the radial dependence of those processes.

In addition to the radial gradient, we also detect a possible richness dependence in color, as the intercept (b) of the fitting results appears to be redder (higher positive value) in richer clusters. This is possibly related to richer and thus more massive clusters containing a higher fraction of red sequence galaxies than the less-massive clusters (Hansen et al. 2009; Sarron et al. 2018; Radovich et al. 2020; Golden-Marx et al. 2023b).

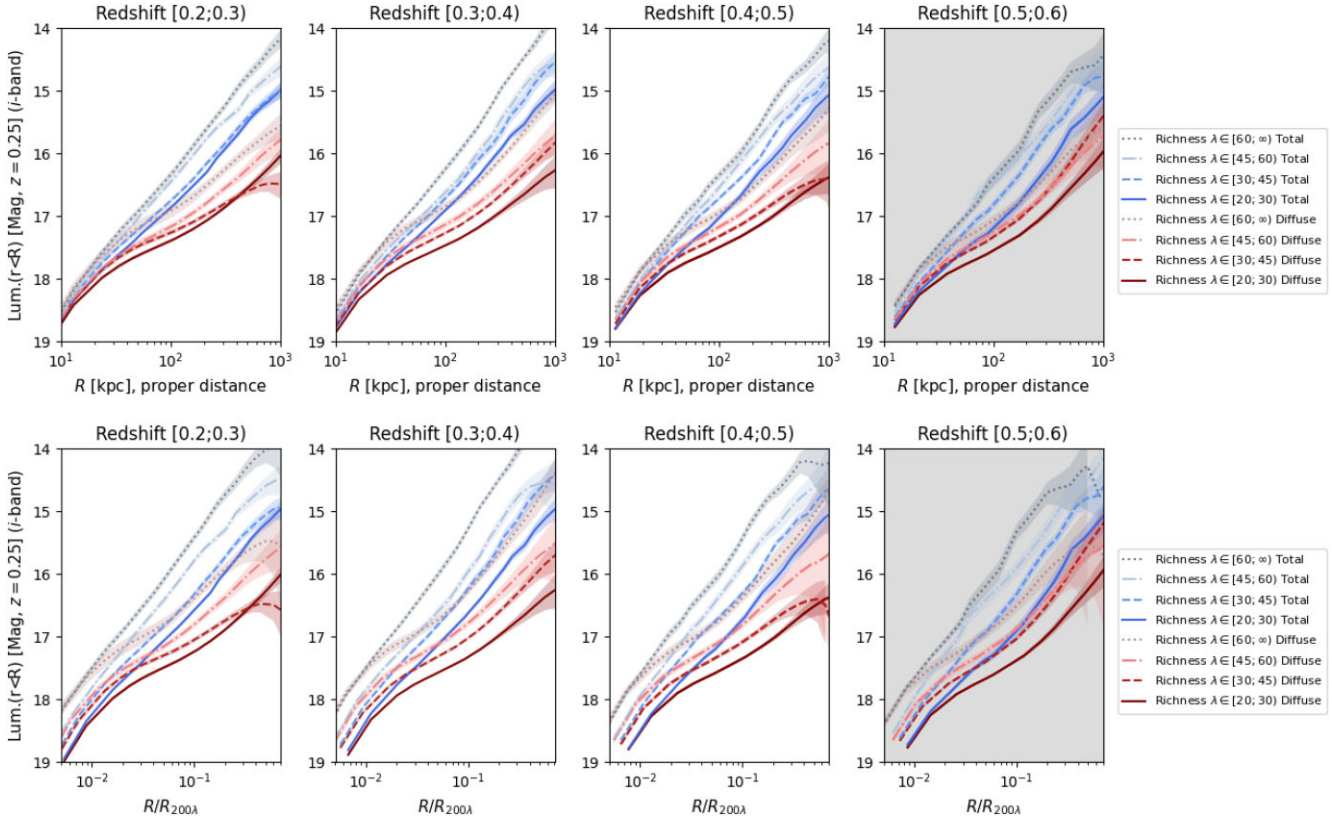

Figure 5. Integrated luminosity (luminosity distance corrected to be the apparent magnitude in the observer frame of $z = 0.25$) as a function of radius (upper panels), or radius scaled by $R_{200\lambda}$ (lower panels). This figure illustrates the luminosity measurements used in our analyses and shows that diffuse luminosity (red lines) and total cluster stellar luminosity (blue lines) increase as the radial range increases. See Section 4 for discussions on the trends manifested in this figure. Each panel shows a different redshift range, while the last redshift panel (redshift 0.5 to 0.6) is coded in a gray color, indicating that this redshift slice may be less reliable because of potential incomplete masking. We note that the last redshift range is not used in quantitative analyses.

4 ICL LUMINOSITY

4.1 Richness and redshift dependence

To further quantify the ICL's richness and redshift dependences, we examine the luminosities of the diffuse light and the cluster's total stellar content. Those luminosities are derived by integrating the SB profile in radial ranges as the following:

$$L(r < R, z = 0.25) = \int_0^R S(r, z = 0.25)\pi r \mathrm{d}r \tag{2}$$

Here, $S(r, z = 0.25)$ is the SB measurements presented in the previous section, which have been luminosity distance-corrected as if it was observed at redshift 0.25. Thus, $L(r < R, z = 0.25)$ is the luminosity measurements enclosed within radius R, but shown as the apparent magnitude in the observer frame of redshift 0.25. We choose this pivot redshift because it is close to the median redshift value in the lowest redshift subsample. Fig. 5 shows the radial profiles of the integrated luminosity as a function of the outbounding R.

There are two significant trends in those luminosity profiles. First, richer and thus more massive clusters contain more diffuse and total light. The richness dependence is observed across the four redshift ranges. Secondly, at small radii, within ∼50 kpc, diffuse light contributes to the bulk of the cluster total stellar light. Outside ∼50 kpc, the cluster's total stellar light increases significantly because of the contribution from cluster satellite galaxies. As a result, diffuse light appears to grow less significantly than the total stellar content with radius. We also show the luminosity radial profiles as a function of radius scaled by $R_{200\lambda}$. The richness/mass dependence of the luminosity becomes even more pronounced in those scaled radius plots.

We further investigate how these luminosities change with redshift and radial apertures. For clusters in a fixed richness range, we derive their luminosities enclosed within 30 kpc and in 30–80, 80–300, and 300–600 kpc annuli. The innermost 30 kpc radial bin is chosen to match the CG size, while the second radial bin, out to 80 kpc (we have experimented with 50, 75, and 100 kpc, and found 80 kpc to be most representative in terms of the redshift trends), is chosen to probe the CG to ICL transition range. Finally, the 80–300 and 300–600 kpc annuli are chosen to probe the extended components of ICL. Those luminosity measurements in apertures/annuli are shown in Fig. 6.

Interestingly, with the lowest richness sample – the clusters in the richness range of 20–30 – we notice that both their diffuse light and total light appear to get brighter towards lower redshift, indicating redshift evolution. In some of the higher richness bins, the luminosities of both the cluster's total and stellar light appear to be getting brighter or unchanged towards lower redshift within 30 kpc. However, outside of 30 kpc, there is no sign of consistent redshift evolution.

To further quantify the richness dependence and redshift evolution in those different apertures, we fit the measurements to the following relation:

$$L(R_0 < r < R_1) = a \times \log_{10}\frac{\lambda_0}{20} + b \times \log_{10}\frac{1+z_0}{1.25} + c. \tag{3}$$

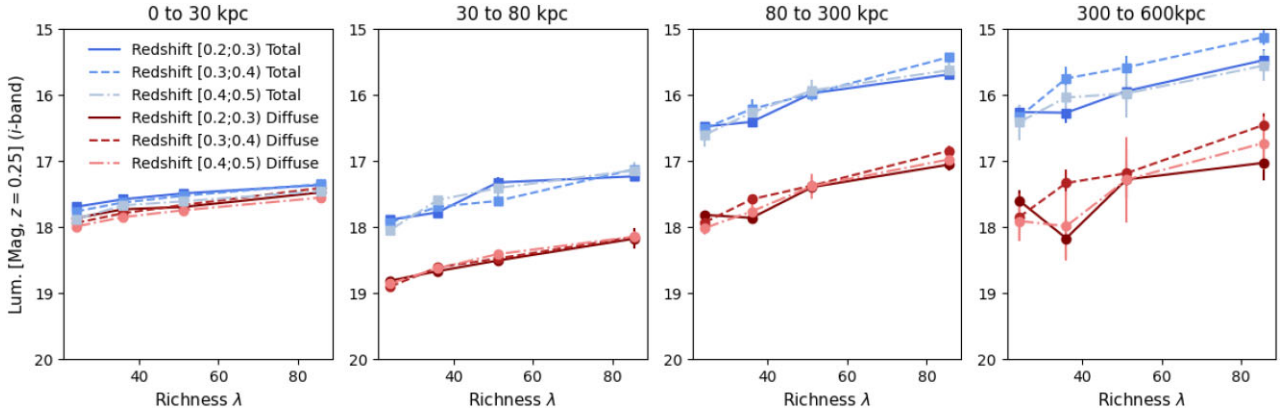

Figure 6. Luminosities (distance-corrected to be the apparent magnitude in the observer frame of $z = 0.25$) enclosed within 4 radial bins (0–30, 30–80, 80–300, and 300–600 kpc). We examine how the luminosities change with redshift and richness. The luminosities of the total cluster stellar content (blue lines) and the cluster diffuse light (CG+ICL, red lines), increase significantly as the cluster's richness increases. However, those luminosities do not appear to change significantly with redshift, except in the lowest richness range and within 30 kpc. See Section 4 for quantitative analyses.

In this relation, the total amount of light ($L(R_0 < r < R_1)$, in the unit of magnitudes) contained within an aperture or annulus, is fitted with a linear relation to the logarithmic values of the cluster subsample's average richness and redshift. The richness and redshift dependences are described by parameters a and b, respectively, and a non-zero value would indicate detection of dependence. In the relation, the pivot richness is chosen as 33, which is the mean richness value of the sample, while the pivot redshift is chosen as 0.25, which is close to the median redshift value in the lowest redshift subsample. Thus, the intercept of the relation, c, can be interpreted as the apparent magnitude of a richness 33 and redshift 0.25 cluster. The fitting of those parameters a, b, and c, is performed with a Markov Chain Monte Carlo method, and the likelihood is constructed from the χ^2 values between the measurements and the relations (using the uncertainties of the measurements as the weighting). Table 2 shows the derived posterior values of the a, b, and c parameters.

The fitted results confirm our fore-mentioned observations. First, the values of a deviate from 0 at very significant levels, between ~ 7 and 16 σ levels in all of the analysed apertures for both the diffuse and the total stellar content. This result confirms the significant richness, and thus cluster mass dependence for the diffuse and total stellar content. Further, the value of a is increasingly negative at large radii, suggesting stronger richness (which is a mass indicator) dependence for the diffuse light as well as the cluster total stellar content.

Also consistent with our fore-mentioned observations, for the diffuse light, the value of parameter b, which quantifies redshift evolution, is consistent with 0 outside 30 kpc. This indicates that when fixing cluster richness, the amount of diffuse light is not obviously increasing (or decreasing) towards lower redshift. Cluster mass may be the main driver for diffuse light evolution in a large radial bin. However, within 30 kpc, the amount of diffuse light appears to be increasing towards lower redshift, suggesting that the amount of stellar light associated with the CG is building up over time. According to the fitting results, the luminosity of the CG becomes brighter by 0.113 mag (calculated from $b \times \log_{10}(1.45/1.25)$) from redshift 0.45 to 0.25 within 30 kpc. This brightening corresponds to a flux increase of 11 per cent. The b value of the diffuse light between 30 and 80 kpc is consistent with 0, but we have also adjusted the 80 kpc outbound range between 50 and 100 kpc, and found that the b value is larger in apertures closer to 30 kpc, indicating possible additional redshift evolution closer to the CG.

For the cluster's total light, b is positive within 30 kpc, also indicating some growth with time (brightening towards lower redshift). Because CG is the dominating component of cluster total light within 30 kpc, the growth in this radial range mostly reflects CG growth. In annuli outside 30 kpc, b is generally consistent with 0, indicating no evidence of significant redshift evolution.

4.2 Volume-limited cluster sample

We further investigate the luminosity evolution of the volume-limited cluster sample discussed in Section 3.3, which helps answer the question of ICL growth when tracking the same cluster's evolution over time. Similarly, we calculate the luminosities enclosed within radial bins for both the cluster diffuse light and total light and show how they change with redshift in Fig. 7. A sign of redshift evolution can be seen within 80 kpc. We do not find evidence of redshift evolution in the rest of the radial bins.

To quantify the redshift evolution of this cluster sample, we also fit their measurements to the following relation:

$$L(z) = L_0 + a \times \log_{10}(1 + z) \quad (4)$$

In this relation, a quantifies the redshift evolution of this cluster sample. A positive value would indicate brightening luminosity over time (towards lower redshift), while a negative value would indicate the opposite. The fitting procedure is performed with the `curve_fit` function of SCIPY, and the derived values and uncertainties of a are noted in Fig. 7.

With both the diffuse light and the cluster total light, we detect positive values of a above the significance level of 1σ within 30 kpc in the CG as well as in the CG to ICL transition region, between 30 and 80 kpc range. In both of the radial ranges, the redshift evolution, indicated by the positive value of a, appears to be larger in the diffuse light than in the cluster total light. This result, together with the results from the richness/redshift subsamples, indicates that the increase in stellar content with time associated with diffuse light is partially driven through the deposition of new material onto the CG and at the CG's outskirt. For the larger radial bins, we again find a to be consistent with 0, and thus, do not find evidence of redshift evolution. It is possible though, that the redshift evolution in those radial bins falls below our measurement limit as the uncertainties of a are large.

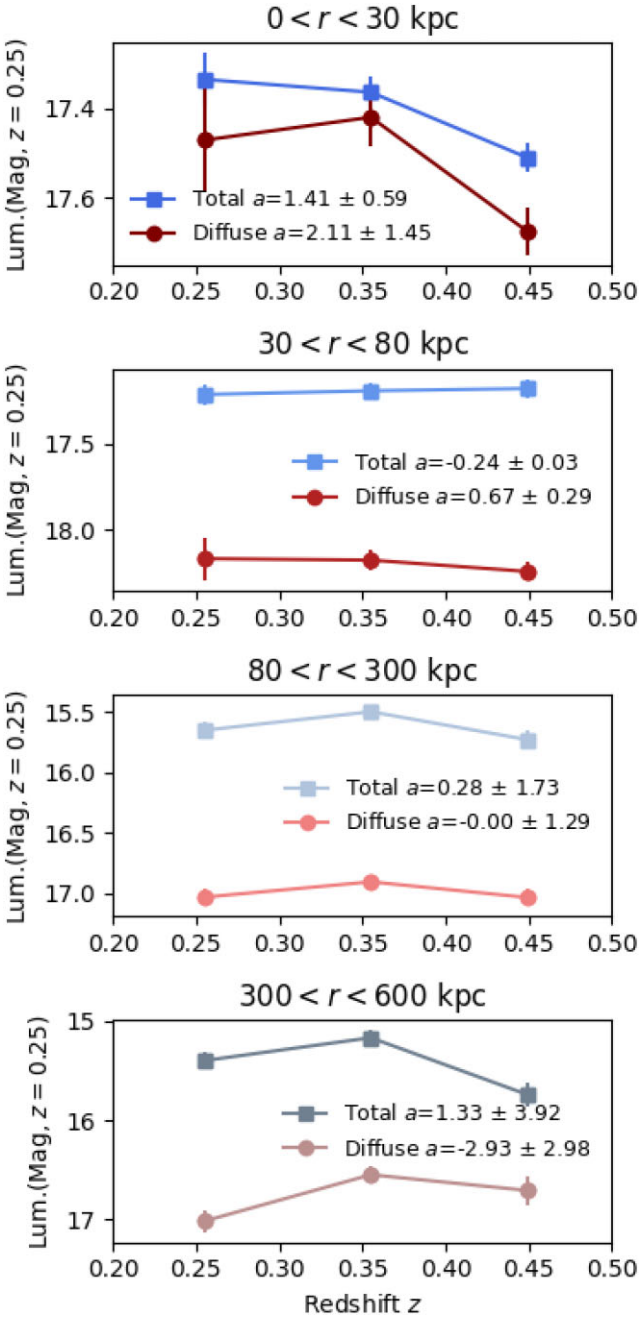

Figure 7. Luminosity (distance-corrected to be the apparent magnitude in the observer frame of $z = 0.25$) as a function of redshift in a volume-limited cluster sample. Again we analyse the brightness enclosed within 4 radial bins (0–30, 30–80, 80–300, and 300–600 kpc, top to bottom panels) and examine how they change with redshift. The luminosities of the total cluster stellar content (blue lines) and the cluster diffuse light (CG+ICL, red lines) both show some signs of becoming brighter over time within 30 kpc, and between 30 and 80 kpc, as indicated by the positive values of the fitted a parameter of equation (4; see discussions in Section 4.2). These trends indicate growth in the CG and in the CG to ICL transition region. In Section 4, we include quantitative analyses of those trends.

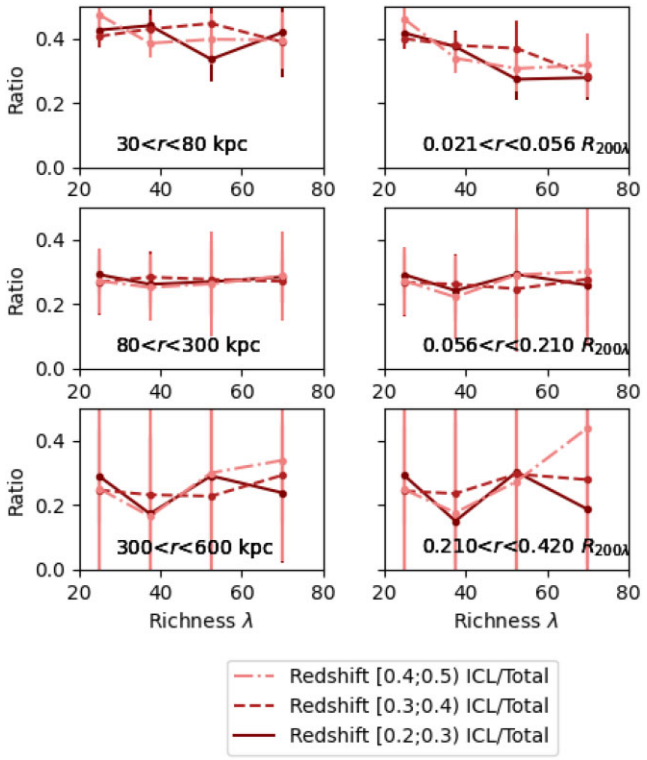

Figure 8. Diffuse fractions in the total cluster stellar content, calculated within physical radii (right column) and scaled radii by $R_{200\lambda}$ (left column). We do not observe consistent redshift or richness-dependent trends (except in the 0.021–0.056 $R_{200\lambda}$ bin) in the measurements. However, the diffuse fractions appear to be dropping from the innermost radial bin to the second. See Section 4.3 for more detailed discussions.

4.3 Diffuse fraction

The fraction of CG and ICL in the cluster's total stellar content is an important quantity (e.g. Behroozi, Wechsler & Conroy 2013; Gonzalez et al. 2013; Ragusa et al. 2022; Joo & Jee 2023). The build-up of the ICL, CG, and cluster total light is not necessarily aligned over time. For example, the ICL and cluster total light may have gone through more or less significant growth in the recent era compared to the CG. Thus, one may observe a change over time in the CG/ICL to cluster total light ratio.

Based on the luminosity measurements, we quantify the fractions of CG and ICL in the total cluster stellar content, with the following equation,

$$\mathrm{Ratio}_{\mathrm{Diffuse}}(R_0 < r < R_1) = \frac{\mathrm{Lum}_{\mathrm{diffuse}}(R_0 < r < R_1)}{\mathrm{Lum}_{\mathrm{total}}(R_0 < r < R_1)} \quad (5)$$

In this equation, $\mathrm{Lum}_{\mathrm{total}}(R_0 < r < R_1)$ enclosed within radius R_0 and R_1 is the luminosity of the cluster's total stellar content derived from its SB, and $\mathrm{Lum}_{\mathrm{diffuse}}(R_0 < r < R_1)$ is the luminosity of the diffuse light derived from its SB. We refer to the ratio of these measurements as the diffuse fraction in this analysis.

Fig. 8 shows these fractions derived for clusters in different redshift/richness ranges. Other than the 0.021–0.056 $R_{200\lambda}$ radial range, the diffuse fraction appears to stay unchanged with richness and redshift, indicating similar richness and redshift dependence between diffuse light and cluster total stellar content. However, the diffuse fraction does appear to decrease after the innermost radius bin, which is averaged to be 40.8 ± 7.0 per cent in the 30–80 kpc range, but decreases to 27.4 ± 9.9 per cent in the in the 80–300 kpc

range and 26.0 ± 25.2 per cent in the 300–600 kpc range. Between 0.021 and 0.056$R_{200\lambda}$ radial range, the diffuse fraction does appear to decrease with richness, but this is likely because of the scaling of $R_{200\lambda}$ with richness; a richer cluster would have a higher $R_{200\lambda}$ value, which excludes more of the CG outskirt with a 0.021$R_{200\lambda}$ cut.

In addition to these trends, Fig. 8 highlights the importance of selecting a radial and cluster mass/richness range when studying diffuse fractions. The fractions depend on how the CG outskirt is included and whether or not the measurements are made in physical radii or radial units scaled by cluster radius. Given the discrepancies in literature reports on diffuse fractions, fair comparisons will need to be made between cluster samples of comparable masses in similar radial scales.

5 SYSTEMATIC EFFECTS AND TESTS

5.1 PSF effect

Because the point-spread function is known to have extended wings (Moffat 1969; King 1971; Racine 1996; Bernstein 2007), it would contribute to the extended low SB features of galaxies or galaxy clusters. The radial scales we probe in this paper are significantly larger than the PSF FWHM of the DES images, therefore we expect minimal PSF contributions to the ICL detection (see discussion in Zhang et al. (2019c)). On the other hand, those contributions may change with redshift given the change of angular distance scale with redshift. Thus, we perform image simulations to probe the possible effect of PSF on the results presented in this paper.

To do so, we convolve a PSF model with an analytical diffuse light profile model and examine the differences before and after PSF convolution. We generate mock 2D images of diffuse light using an analytical model, setting the angular scale of the analytical diffuse light profile models at four redshifts, 0.25, 0.35, 0.45, and z = 0.55 (but without adjusting their SB level as we are only looking at before-and-after PSF convolution differences). These 2D images are then convolved with a 2D PSF image model. Both the analytical models and the PSF models are based on the DES-Year1 measurements in Zhang et al. (2019c) in r-band, as the PSF models have similar large radial behaviors outside 2 arcsec. We then derive the SB measurements in radial bins before and after PSF convolution. The results are shown in Fig. 9.

The top panel shows the flux changes of the profiles before and after the PSF convolution for the three profiles at different redshifts. PSF convolution flattens the central regions of those profiles limited by the pixel scale of the images (0.263 arcsec pixel scale). The middle panel of Fig. 9 shows the relative changes in those profiles before and after convolution. Outside of 10 kpc, PSF convolution has a minor effect on SB measurements which change by less than 10 per cent, but the change depends on redshift. Outside of 100 kpc, PSF effects appear to be negligible for all of the four redshifts, which is less than 1 per cent at 100 kpc for $z = 0.55$.

As with the integrated (within radius) brightness measurements, similarly, the PSF effect appears to be negligible if integrating to 20 kpc, affecting less than 5 per cent of the flux measurement, or around 2 per cent if integrating to 30 kpc. Within 10–20 kpc, the PSF may affect the CG flux measurements by up to 12 per cent, depending on the redshift. Within 10 kpc, the integrated luminosity needs to be carefully interpreted due to the PSF effect.

We conclude that PSF effect alone cannot account for the redshift evolution in the diffuse light luminosity measurement within 30 kpc, which shows a change of ∼0.2 mag, or ∼ 20 per cent in flux from redshift 0.45 to 0.25 (Section 4). With a carefully designed CG aperture (30 kpc in this analysis), our luminosity redshift evolution results should be minimally affected by the PSF effect.

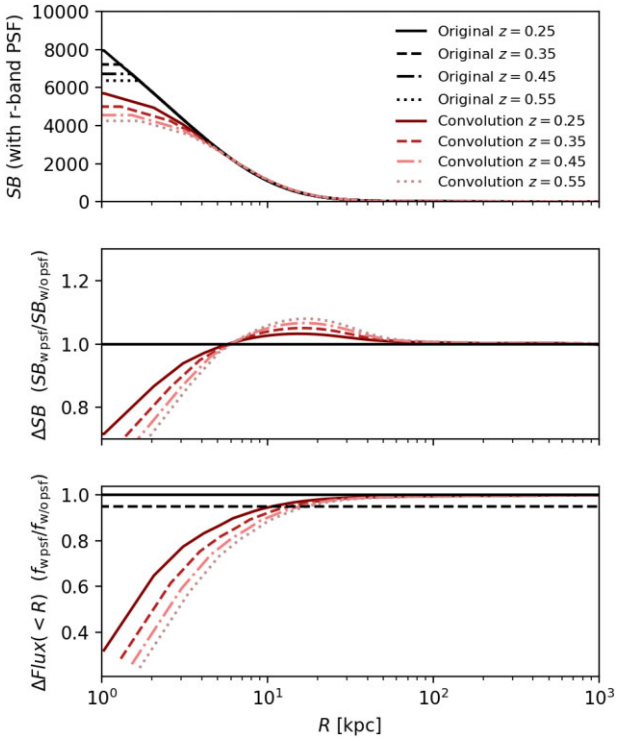

Figure 9. Testing the effect of PSF on SB and luminosity measurements. Upper panel: diffuse light SB models are convolved with a PSF model at different redshifts. The PSF flattens out the SB distribution in the centre. Middle panel: Relative change in SB after the diffuse light profile models are convolved with a PSF model. The changes are most significant within 10 kpc. Lower panel: Relative changes in luminosity (derived by integrating the SB profiles radially as described in Section 4) after a PSF model convolution. The integrated luminosity is most affected within 20 kpc.

5.2 Masking magnitude limit

The masking magnitude limit we use for this work varies with redshift. This may affect the results of this paper when cluster galaxies below the masking limit contribute a noticeable amount of light to the diffuse light measurements. We acknowledge this issue as a limitation in our analysis, as we do not explicitly account for the contributions from the fainter cluster member galaxies below the masking limit.

We test how much our results may have been affected by these magnitude limits. In this test, we redo the measurements of the diffuse light using a masking magnitude that is fainter by 0.7526 mag (or masking to 0.1$L*$ of the cluster luminosity function), and compare the results to those from the fiducial analyses presented earlier. We have not applied this deeper magnitude limit in our fiducial analysis because of the increasingly incomplete galaxy detection associated with this magnitude limit, which would render the results in the redshift 0.4–0.5 bin less reliable. Nevertheless, we show the SB measurements with this deeper magnitude limit and the comparison to the fiducial analysis in Figure 10.

Indeed, using a deeper masking limit notably reduces the SB measurements of the diffuse light throughout the redshift and richness bins. Outside of 100 kpc, the reduction in flux consistently reaches a ∼ 10 per cent level, although there are significant fluctuations

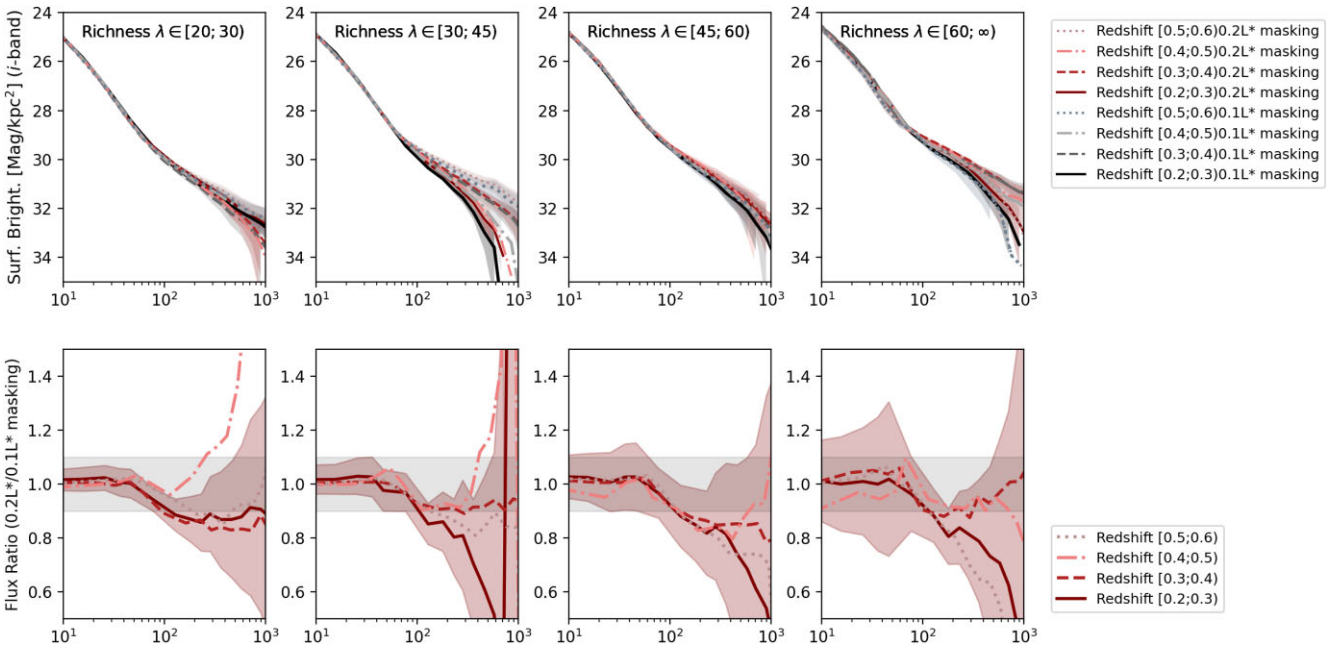

Figure 10. Diffuse light profiles derived when using a deeper masking magnitude limit (upper panels) and the relative differences to the fiducial measurements presented in previous sections (lower panels). The SB measurements outside 100 kpc can be lowered by 10 per cent when using a deeper masking magnitude, which removes more contamination from the faint cluster satellite galaxies.

as indicated by the uncertainties. Given that satellite galaxies 2.5–5 times brighter than the ICL in this radial range (Section 4) are excluded, a reduction of 10 per cent in flux means that the deeper magnitude is only further removing 2 per cent to 4 per cent of the faint cluster satellite galaxy contribution. A deeper masking magnitude is unlikely to significantly further reduce ICL brightness unless there is a noticeable upturn in the cluster galaxy luminosity function at the faint end (e.g. Lan, Ménard & Mo 2016).

Other than the masking limit as well as the PSF effect, there are other additional effects that influence our results. Another issue related to masking is that the masking aperture does not enclose all of the light from cluster satellite galaxies. A galaxy's light can reach tens or even hundreds of kpcs. In Zhang et al. (2019c), we found that the aperture of masking only affects diffuse light measurements at a percentage level. In addition, in this analysis, we have adjusted the masking radius to be 3.5 Kron radii rather than 2.5 Kron radii which will further reduce the effect. Moreover, the cluster galaxy luminosity function may evolve with redshift. However, recent literature studies find that the redshift evolution of the cluster galaxy luminosity function is very mild at most (e.g. Hansen et al. 2009; Sarron et al. 2018; Zhang et al. 2019b; Puddu et al. 2021).

5.3 Sky background

Accurate diffuse light measurements require accurate evaluation and removal of the sky background in optical images. Similar to Zhang et al. (2019c), in this paper, the images we use have removed sky background that is estimated over the whole field-of-view (FOV) of DECam, approximately 3 deg^2, using a PCA method (Bernstein et al. 2017b). Given that one galaxy cluster, even at redshift 0.2, only makes up a very small area in the DECam FOV, the sky background estimation is not sensitive to the presence of galaxy clusters, thus avoiding a background overestimation issue that often plagues ICL measurements. Zhang et al. (2019c) tested the DECam FOV PCA background evaluations for ICL measurements, and it was shown that the PCA sky estimations at the cluster centres and at a large cluster radius (1.36 arcmin from the cluster centre) are highly consistent.

After removing the full FOV sky background level, the images still possess a residual background. Since we average the measurements for several hundreds and sometimes several thousands of clusters, we estimate a residual background for those averaged measurements, through processing 'sky randoms' that track the area coverage of the cluster sample. A SB profile of the sky randoms is acquired using the same procedure of the cluster measurements. Those 'random' profiles are subtracted from the 'raw' cluster measurements to acquire the final cluster-related measurements. The top panel of Fig. 11 illustrates the procedure.

In Fig. 11, because of the residual background, the 'raw' cluster measurements still have a SB level of $\sim$2 kpc^{-2} in flux measured at large radii ($\sim$2 Mpc), but this residual is also present in the 'random' measurements. After subtracting the randoms, the final cluster measurements fluctuate around 0 at very large radii ($\sim$2 Mpc). Note that in Fig. 11, we are showing the measurements in DES 'flux' (10^{-12} of a maggy), where the 'flux' used here is a linear measure of an object's brightness, as opposed to the logarithmic 'magnitude' unit of brightness with the following relation mag = 30–2.5 $\times$ log$_{10}$(flux).

We note the importance of using random catalogues that faithfully trace the sky coverage of the redMaPPer cluster catalog. The raw profile measurements of randoms in Fig. 12 are sensitive to the selection of the random catalogues (and thus the redMaPPer cluster catalogues). These two catalogues are selected to avoid sky regions that contain bright foreground galaxies and stars – at least 0.2 deg away from their centres. If we adjust the distance cuts to 0.3 or 0.4 deg, the random's profile value would become lower, indicating different 'residual' background levels.

Finally, a crucial difference between this paper and Zhang et al. (2019c) is that we use the coadded images from the DES directly,

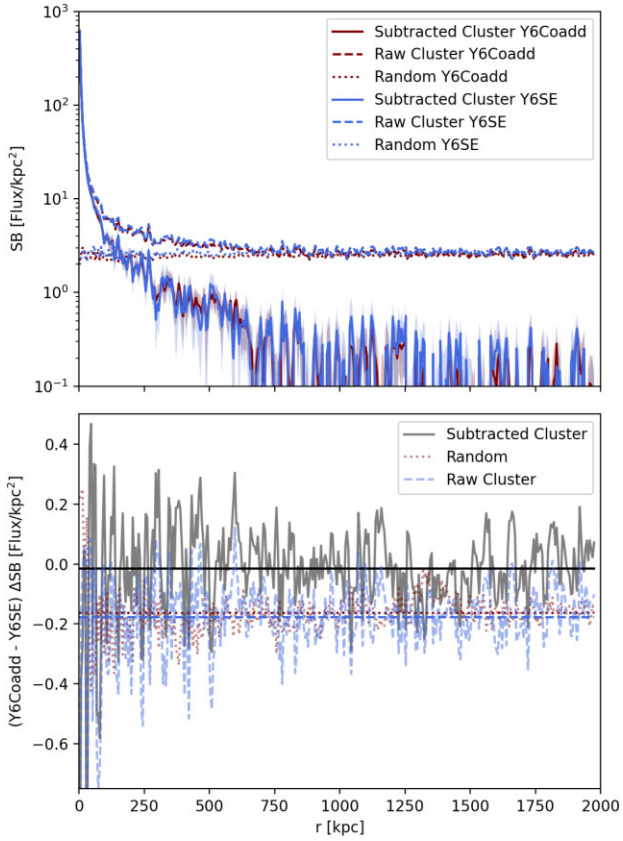

Figure 11. Upper panel: Diffuse profiles derived from DES special coadded images (red lines, Y6ACoadd, fiducial results in this paper) vs. those derived from single epoch images as in Zhang et al. 2019 (Y6SE, blue lines). Lower panel: Differences in these profiles. These two approaches yield consistent SB measurements to an accuracy level of over 30 mag kpc^{-2} in terms of raw diffuse light and random profile measurements. After random profile subtractions, the differences vanish at a SB level of 40.5 mag kpc^{-2}.

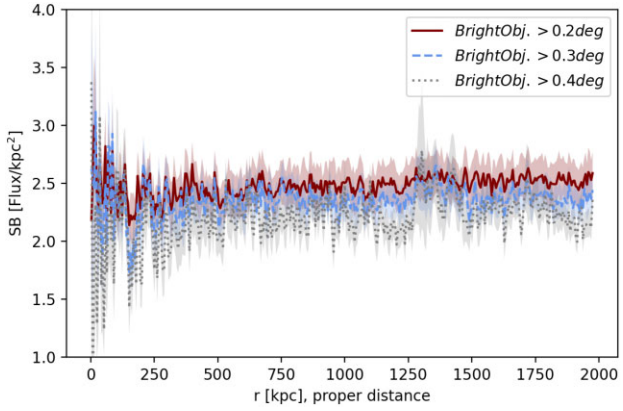

Figure 12. SB of the randoms when using different distance cuts to bright objects in the sky. Our analysis requires the bright objects identified in a DES masking file to be 0.2 deg away from the cluster centre. Using further cuts would lower the SB measurements of randoms because of less contamination from the bright objects.

which is based on coadding single epoch images after the PCA sky background subtraction. The DES coadd images (the 'no-bkg' coadd images in the DES data release, which did not subtract local background) are based on the procedure in Zhang et al. (2019c) to better preserve low-SB features.

To test that the DES coadds are indeed suitable for detecting ICL, we separately process the redshift 0.2–0.35 clusters by coadding single epoch images using the same procedures in Zhang et al. (2019c) and compare the measurements to the DES special coadd-based measurements. Their differences are shown in Fig. 11.

The raw SB measurements of those clusters and the randoms from both sets of images are offset at a flux level of 0.2, corresponding to a SB level of 31.7 mag kpc^{-2}. Those raw measurement differences between the two coadding procedures are likely caused by pixel weighting differences. After the random subtraction, the measurements are similar at a surface flux level of 0.015, which means that the two methods are similar to a SB level of 40.5 mag kpc^{-2}, and thus highly consistent.

5.4 Galaxy cluster mis-centring

As described in Section 2, the redMaPPer cluster sample provides a most likely CG candidates for each cluster, but sometimes (∼20%) a wrong CG is identified as the top CG candidate. This kind of mis-centring may affect the interpretation of the CG and ICL measurements presented in this paper. The redMapper mis-centring effect has been investigated with multiwavelength data (Zhang et al. 2019a; Bleem et al. 2020), and recently, Kelly et al. (2023) calibrated the mis-centring statistics for the DES Year 3 redMaPPer cluster sample using X-ray data. Specifically, they characterized the mis-centring distribution of redMaPPer cluster sample by assuming that the well-centred clusters makes up a fraction of the sample, with the fraction denoted as the ρ parameter. For the mis-centred clusters (fraction of $1-\rho$), Kelly et al. (2023) modelled the offset distance between the true centres and the REDMAPPER-identified centres with a gamma distribution with a shape parameter of 2, and a 'rate' parameter of $\tau \times R_\lambda$ ($R_\lambda = (\lambda/100)^{0.2} h^{-1}$Mpc). Thus, redMaPPer cluster's mis-centring distribution, can be fully described by the ρ and τ parameters. Kelly et al. (2023) found the mis-centring statistics to be consistent between low and high richness clusters, but detected a potential change (still within 2σ significance level) between the redshift 0.2 and 0.4 and 0.4 and 0.65 cluster sub-samples. In this section, we estimate the potential impact that mis-centring may have on interpreting the CG and ICL richness and redshift dependence presented in this paper.

The mis-centring statistics (characterized by the ρ and τ parameters) in Kelly et al. (2023) appear to be consistent at low and high cluster richness. However, because the mis-centring distance distribution is scaled by $\tau \times R_\lambda$, a richness dependence is introduced through the R_λ parameter. To investigate how mis-centring would affect the interpretation of our ICL measurements, we build an ICL model, and then use the mis-centring constraints from Kelly et al. (2023) to 'mis-centre' these ICL models. We model the CG and ICL of well-centred clusters with two Sersic components (best-fitting results to our CG+ICL measurement in the redshift 0.2–0.3, richness 30–45 bin) – one component with Re =12.7 kpc and index 2.26 to mimic the measurements at the core (the CG) and another component with Re=1.11 Mpc and index 2.85 to mimic the diffuse component. We then 'mis-centre' the 'diffuse' component, by assuming 20 per cent the clusters are mis-centred ($\rho = 0.80$), with the mis-centring offset following a gamma distribution characterized by $0.21 \times R_\lambda$ ($\tau = 0.21$), with R_λ derived from $\lambda = 25$ and $\lambda = 50$,

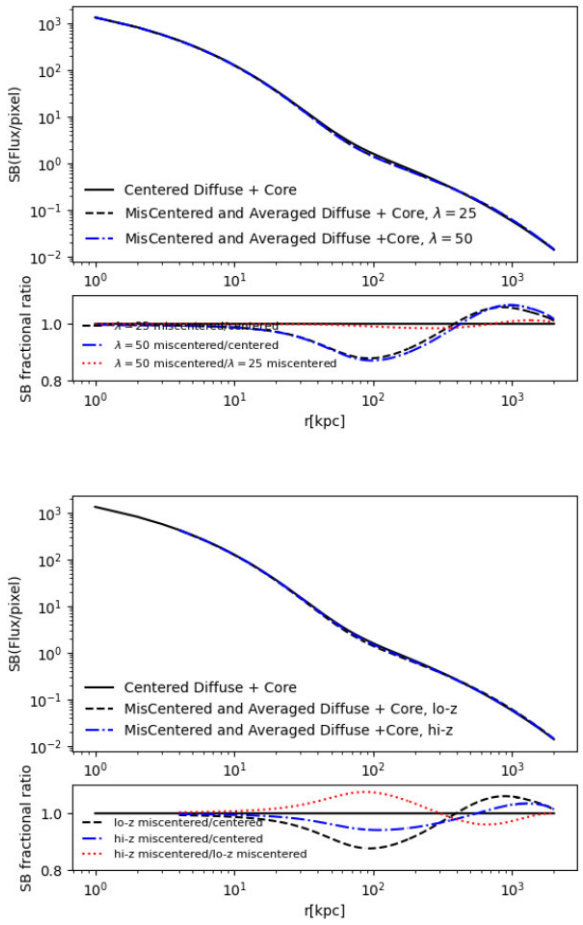

Figure 13. Well-centred and Mis-centred CG and ICL models. Upper panel: CG and ICL models mis-centred according to the redMaPPer mis-centring distribution constraints in Kelly et al. (2023), assuming cluster richness to be 25 and 50 respectively. Lower pannel: CG and ICL models mis-centred according to the redMaPPer mis-centring distribution constraints at redshift 0.2–0.4 and 0.4–0.65, respectively. Overall, compared to the centred ICL model, mis-centring shifts the measurement of ICL in the inner part of the clusters to a larger distance – lowering the measured SB level of ICL around 100 kpc, but increasing the ICL light SB level at a larger distance. We find that mis-centring has a negligible effect on interpreting the richness-dependence of the CG and ICL measurement, but a small ($\sim<5$ per cent) effect on interpreting redshift-dependent measurements. See Section 5.4 for detailed discussions.

respectively for low and high richness models. In addition, we assume that even when the cluster is mis-centred (i.e. picked a 'wrong' galaxy as the CG), this identified centre still has the same core component with the real CG (same brightness, with $Re = 12.7$ kpc and $n = 2.26$), as the redMaPPer algorithm always pick a bright galaxy as the centre. We build a new CG and ICL model by azimuthally averaging over the centred and mis-centred CG and ICL models, adopting the approach in cluster weak lensing analyses (e.g. McClintock et al. 2019) that a well-centred model is integrated over a mis-centring offset distribution, weighted by the fraction of clusters that are mis-centred.

The upper panel of Fig. 13 shows the well-centred CG and ICL model, as well as the new models after incorporating the mis-centring distributions. Compared to the centred model, mis-centring shifts the measurement of ICL in the inner part of the clusters to a larger distance, lowering the measured SB level of ICL around 100 kpc but increasing the ICL light SB level at a larger distance. However, the mis-centred models with richness values of 25 and 50 are highly consistent, with a maximum SB difference less than 2 per cent throughout the 0–2 Mpc radial range. This level of difference is negligible compared to the ICL SB measurement differences in different richness bins (Sections 3 and 4).

We then investigate how cluster mis-centring affects the interpretation of the redshift-dependent CG and ICL measurements. We mis-centre the CG+ICL model with the Kelly et al. (2023) constraints at redshift 0.2–0.4 with $\rho = 0.80$ and $\tau = 0.21$, and at redshift 0.4–0.65 with $\rho = 0.92$ and $\tau = 0.33$, fixing the cluster's richness to be 30 for both models. The lower panel of Fig. 13 shows these mis-centred models. Because of a lower mis-centring fraction, mis-centring affects the high-z model less dramatically. Comparing the high-z and low-z models, the integrated fluxes of the high-z model is higher than the low-z model by 0.99 per cent, 5.3 per cent, or 4.1 per cent when integrating over the radial ranges of 0–30, 30–80, or 80–300 kpc, but lower by 2.5 per cent when integrated over the 300–600 kpc range. If the underling CG and ICL model stays the same, the change in the mis-centring statistics between redshift 0.4 and 0.65 and redshift 0.2 and 0.4 would create a counter-growth (brighter ICL at higher redshift) in the 0–30, 30–80, and 80–300 kpc radial ranges, and a growth effect (brighter CG+ICL at lower redshift) in the 300–800 kpc radial range. Note that because we use a smaller redshift range ($0.2 < z < 0.5$) in this paper, we expect a even smaller redshift-dependent mis-centring effect on our cluster sample.

Nevertheless, these fractional changes are smaller than the values/uncertainties of the measurement changes in CG and ICL luminosity between redshift 0.45 and 0.25, that we have inferred and listed in Table 2 ($b \times \log(1.45/1.25)$) for the 0–30 kpc (11 ± 3 per cent) and 300 and 600 kpc ($-8.6 \pm 19.8\%$) radial ranges, but comparable to the uncertainties of the measurements for the 30–80 kpc (-0.06 ± 3.32 per cent) and 80–300 kpc (-0.60 ± 6.81 per cent) radial ranges. For the latter radial ranges, it is possible that the lack of ICL growth that we are measuring is due to the true ICL growth rate being low ($\sim<5$ per cent level) and countered by the evolution of redMaPPer mis-centring over redshift. It would be interesting to carry out a full forward-modelling analysis of redMaPPer to study ICL growth in the future, accounting for the effect of redMaPPer mis-centring.

6 DISCUSSION ON REDSHIFT EVOLUTION

6.1 Comparison to simulation

To gain theoretical insights into the evolution of ICL, we turn to the IllustrisTNG simulation suite (Marinacci et al. 2018; Naiman et al. 2018; Nelson et al. 2018; Pillepich et al. 2018; Springel et al. 2018; Nelson et al. 2019) to examine how the diffuse stellar components of galaxy clusters change with cluster mass and redshift. This has already been a subject of investigation in Pillepich et al. (2018).

Our analysis here is based on the TNG300-1 simulation, which has the largest volume (300 Mpc^3) in the IllustrisTNG simulation suite, and also the highest simulating resolution among the 300 Mpc^3 volume series. The TNG300-1 simulation contains 263 dark matter haloes above the mass threshold of $6 \times 10^{13} \mathrm{M}_\odot\, h^{-1}$ at redshift 0.27. It has an advantage over the smaller-volume simulations (i.e. the TNG 100 and 50 Mpc^3 series), which contain much smaller samples of cluster-sized dark matter haloes despite their higher simulation resolutions.

We select the redshift snapshots at 0.27, 0.42 and 0.58 for this analysis, to represent the redshift range studied in this paper. In

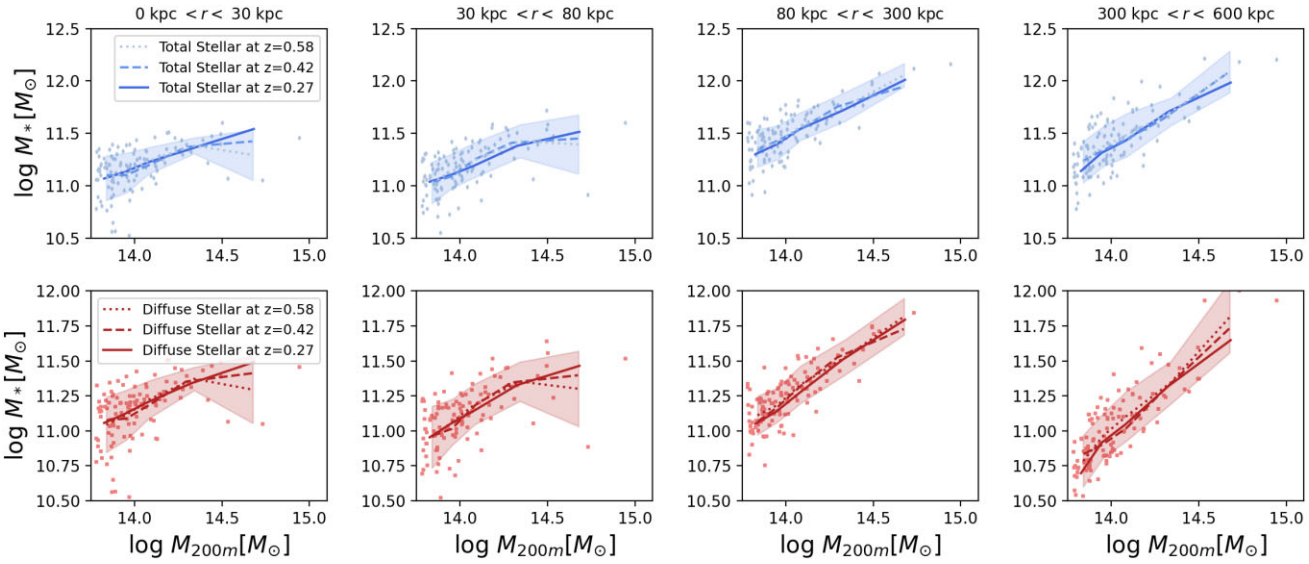

Figure 14. The stellar mass of diffuse light and of the cluster's total stellar content in the IllustrisTNG 300–1 simulation, as a function of the host halo's mass. The different lines indicate the running means in different redshift snapshots. These stellar mass–halo mass relations do not seem to vary with redshift. However, those relations depend on the spherical radial apertures used to calculate the stellar masses, and are steeper in large radial ranges.

each redshift snapshot, we select dark matter haloes with $M_{200\mathrm{m}}$ above $6 \times 10^{13} \mathrm{M}_{\odot}\, h^{-1}$ as 'galaxy clusters'. After cutting dark matter haloes that are too close to the simulation box boundaries (within 20 cMpc h^{-1}[6]), we are left with 205, 155, and 115 dark matter haloes respectively in the three redshift snapshots. Those dark matter haloes will be referred to as galaxy clusters in the rest of this analysis. For each simulated cluster, centred on its weighted mass centre, we select the diffuse stellar particles contained in 3D spherical distance apertures and compute their total stellar masses. Those stellar masses are shown together with the host halo mass in each redshift snapshot in Fig. 14. In addition to the diffuse stellar component, we also included the dark matter halo's total stellar content (subhalo+diffuse) within those spherical radial apertures for comparison.

In this simulation, both the diffuse and total stellar components of galaxy clusters steadily increase as the galaxy cluster mass increases. This mass dependence grows steeper in larger spherical radial apertures. On the other hand, examining the mean of those stellar masses (M_*) as a function of halo mass ($M_{200\mathrm{m}}$), there does not appear to be tangible differences in different redshift snapshots, indicating no redshift evolution.

To further quantify the mass dependence and redshift evolution in the simulation, we fit each haloes's stellar masses M_*, halo masses $M_{200\mathrm{m}}$, and redshifts z_0 to the following stellar–mass and halo–mass relation.

$$\log_{10} M_* = a \times (\log_{10} M_{200\mathrm{m}} - 14.0) + b \times \log_{10} \frac{1+z_0}{1.25} + c. \quad (6)$$

This relation is similar to the one adopted in Section 4, substituting richness-dependence for mass dependence.

The fitted constraints on the relation are listed in Table 3. In the relation, parameter a quantifies the mass dependence of the stellar masses. Its value is positive in all of the radial bins, and becomes even more positive at larger radii, in agreement with the steeper mass dependence we have seen in Fig. 14. On the other hand, parameter b quantifies the redshift evolution. Its value is consistent with 0 in all of the bins, indicating a non-detection of redshift evolution. Overall, our results confirm the findings in Pillepich et al. (2018; as well as in Golden-Marx et al. 2023a) that did not find redshift evolution in the stellar–mass to halo–mass relation of galaxy clusters, in either the diffuse component or the subhalo component. However, both stellar mass components scale strongly with halo mass. We note that in small radial ranges, the properties of halo CGs or massive galaxies in the simulation do not always match observations (e.g. Pillepich et al. 2018; Li et al. 2019; DeMaio et al. 2020; Cannarozzo et al. 2023). Nevertheless, those simulation results qualitatively agree with our measurements in the large spherical radial ranges outside of 80 kpc.

Table 3. Constraints on parameters in the simulation stellar mass to halo mass relation $\log_{10} M_* = a \times (\log_{10} M_{200\mathrm{m}} - 14.0) + b \times \log_{10} \frac{1+z_0}{1.25} + c$.

	a	b	c
$r \leq 30$ kpc Total	0.51 ± 0.20	-0.08 ± 1.22	11.17 ± 0.07
$r \leq 30$ kpc Diffuse	0.51 ± 0.21	-0.11 ± 1.21	11.16 ± 0.07
$30 \leq r \leq 80$ kpc Total	0.63 ± 0.21	0.17 ± 1.22	11.14 ± 0.07
$30 \leq r \leq 80$ kpc Diffuse	0.67 ± 0.21	0.03 ± 1.21	11.08 ± 0.07
$80 \leq r \leq 300$ kpc Total	0.81 ± 0.20	0.36 ± 1.22	11.45 ± 0.07
$80 \leq r \leq 300$ kpc Diffuse	0.89 ± 0.21	0.44 ± 1.19	11.20 ± 0.07
$300 \leq r \leq 600$ kpc Total	0.99 ± 0.21	0.53 ± 1.21	11.34 ± 0.07
$300 \leq r \leq 600$ kpc Diffuse	1.11 ± 0.21	0.65 ± 1.22	10.93 ± 0.07

6.2 Comparison to literature

Perhaps the most surprising result from this paper is the relative lack of ICL evolution at a radius larger than 80 kpc. Many analyses characterizing CG and ICL growth, including the work of the co-authors of this paper, have predicted significant growth of the ICL (e.g. Behroozi et al. 2013; Zhang et al. 2016; Contini et al. 2018; Golden-Marx et al. 2022) as a mechanism to explain the relatively slow CG growth observed below redshift 1.5 (e.g. Stott et al. 2010; Lidman et al. 2012; Lin et al. 2013). However, we do find signs of diffuse light redshift evolution in the CG as well as in the CG to ICL transition within 80 kpc.

[6]c in cMpc/h stands for comoving distance.

Prior to this analysis, there have been few works that analyse large samples of ICL profiles over a broad range of redshift to directly quantify their redshift evolution. One of the most comparable literature studies to our work is presented in DeMaio et al. (2020), which analyzed 42 clusters in the redshift range of 0.05–1.75. DeMaio et al. (2020) measured the BCG and ICL growth out to about 100 kpc from the cluster centre, and found that the stellar masses of BCG and ICL increase more rapidly than the cluster's total mass from redshift 1.5 to the present. They conclude that BCG+ICL growth is not solely driven by cluster mass growth. In this analysis, we indeed observe that the CG and ICL luminosity increases mildly within 30 kpc.

There are some differences between our work and that of DeMaio et al. (2020). DeMaio et al. (2020) find that the ICL stellar mass amplitude is 2.08 ± 0.21 times higher at redshift 0.4 than at redshift 1.55, when examining the 10−100 kpc range. While in this paper, we find evidence of ICL growth by 11 per cent within 30 kpc of the cluster centre from redshift 0.45–0.25. In our analysis, the results are derived for clusters in a time span of roughly 1.7 Gyr (redshift 0.45–0.25). The ICL growth observed in DeMaio et al. (2020) occurs over an extended period of 4.97 Gyr from redshift 1.55 to 0.4. Interpolating from their measurements, the ICL measured between 10 and 100 kpc can grow by 37 ± 3.7 per cent in 1.7 Gyr, significantly higher than the $11^{+3.1}_{-3.0}$ per cent measured in our work within 30 kpc of the cluster centre where we see the most growth. On the other hand, DeMaio et al. (2020) have noted a slowdown in the BCG and ICL growth, such that from redshift 0.4 to 0.1, there's no change in the diffuse light stellar mass (between 10 and 100 kpc) to halo mass relation.

Furthermore, in our work, we do not find signs of ICL growth outside 80 kpc. On the other hand, Golden-Marx et al. (2023a) studied ICL growth from redshift 0.8 to 0.2, but also do not find much evidence for ICL growth. Golden-Marx et al. (2023a) defines ICL with a large radial aperture of between 50 and 300 kpc and those results are based on the same imaging data set and processing method as in this paper. In both Golden-Marx et al. (2023a) and this work, we are limited by the PSF resolution (as discussed in Section 5) to probe a smaller radial range such as 10–30 kpc. Combining the findings from DeMaio et al. (2020); Golden-Marx et al. (2023a) and this work, we speculate that the CG, as well as the region close to the CG within 100 kpc, rather than the ICL at a very large cluster radius, holds the key for explaining CG and ICL growth. However, the growth may not be very noticeable below redshift 0.45.

Another comparable analysis is from Furnell et al. (2021), which studied ICL growth over the redshift range of 0.1 to 0.5, using 18 X-Ray selected clusters with Hyper Suprime Cam Subaru Strategic Program observations. Using a radial aperture of R_{500} and a SB limit of 25 mag arcsec^{-2}, Furnell et al. (2021) find that the ICL fraction increases by a factor of 2–4 over the 0.1–0.5 redshift range with no obvious mass dependence. However given that the ICL definition in Furnell et al. (2021) is based on a SB limit, a radius aperture of R_{500} that scales with cluster mass, as well as a 'divot' correction due to background subtraction in the images, it is possible that the ICL definitions in their and our analyses are not directly comparable.

7 SUMMARY AND PROSPECTS

In this paper, we present measurements of the circularly averaged CG and ICL radial profiles using the full 6 years of DES data. The major findings from those measurements can be summarized as the following:

(1) the diffuse light (CG+ICL) extends to 1 Mpc in the redshift range of 0.2−0.5 investigated in this analysis. Prior to this analysis, multiple studies have already detected ICL in the several hundreds of kpc to Mpc radial range, which includes both 'stacking' based analysis like this paper (e.g. Zibetti et al. 2005; Chen et al. 2022), and deep imaging studies of individual galaxy clusters (e.g. Krick & Bernstein 2007; Kluge et al. 2021; Golden-Marx et al. 2022). Our finding again showcases the wide radial reach of ICL. There may be much to study with the radial properties of ICL.

(2) We find that the diffuse light SB and luminosity strongly depend on richness − a galaxy cluster mass proxy. This dependence is stronger at large radii outside of 50 kpc from the cluster centre. As richness scales with cluster mass (the richer a cluster is, the more massive it is likely to be), the richness and thus cluster mass dependence appears to be the major factor behind the differences between diffuse light observations in different subsamples, as their radial profiles scale well with the cluster's radius ($R_{200\lambda}$) and their fractions in the cluster's total stellar luminosity appears to be richness-independent. The results agree with previous studies that find a strong mass correlation between ICL luminosity or stellar mass, or a possible correlation between the cluster mass distribution and ICL SB (e.g. Montes & Trujillo 2019; Huang et al. 2020; Kluge et al. 2021; Sampaio-Santos et al. 2021; Ragusa et al. 2022).

Perhaps most interesting of all to cluster cosmology studies, this finding, again, suggests the potential of ICL as a cluster mass proxy (Golden-Marx et al. 2023a), or to help improving cluster finding algorithms (Huang et al. 2022). Cosmology studies based on galaxy cluster abundance measurements have long emphasized the importance of developing accurate and precise cluster mass proxies (i.e. galaxy cluster observables that scale well with masses), because a mass proxy with low scatter to the cluster's true mass can significantly reduce the requirement for follow-up observations, and thus reduce the derived uncertainties on cosmological parameters such as Ω_m and σ_8 (Rozo et al. 2010). Further, the precision of those cosmology studies also depends on having an accurate mass proxy that is not affected by the cluster's large-scale structure environment (Wu et al. 2022).

We note that a cluster mass proxy does not need to be solely based on ICL measurements. Past analyses have developed cluster mass proxies by combining various measurements of a galaxy cluster, as was done with the richness estimation used by the redMaPPer algorithm. We think that it will be particularly interesting to incorporate diffuse light quantities in developing cluster mass proxies or cluster finding algorithms (Huang et al. 2022), potentially using a Machine Learning algorithm (Lin et al. 2022) combining a few cluster measurement quantities.

(3) Perhaps with a bit of a surprise, we find that the diffuse light at large cluster radii (outside of 80 kpc from the cluster centre) is not evolving much with redshift (when fixing richness) in the 0.2–0.5 range. Closer to the cluster centre, within 80 kpc, we have found some evidence that the diffuse light's luminosity increases with time (towards lower redshift). We speculate that ICL build-up may be more pronounced closer to the CG, while at large radii, on the scale of hundreds of kpc, ICL build-up is more in tune with the cluster mass build-up, which also explains the stronger cluster mass dependence at large radii.

In the context of CG and ICL co-evolution studies, many (including the authors of this paper) have speculated a more rapid growth of ICL than the BCGs below redshift 1. Given that ICL and CG is often vaguely defined in those studies, our findings suggest that ICL growth may happen at a much smaller radius (i.e. in the CG or at the CG outskirt) than we previously expected. Our finding of little redshift evolution at large cluster radius is in agreement with the hydrodynamic simulation study of IllustrisTNG (Pillepich et al.

2018), which finds little redshift evolution in diffuse light stellar mass once the cluster's halo mass is fixed.

(4) We have measured additional properties of ICL: the colour profile of diffuse light has a radial gradient, which becomes bluer at a larger radius, and also bluer in less rich/massive clusters. In addition, the diffuse light SB profiles appear to be 'self-similar' after scaling by the cluster radius, and that ICL fraction in the total cluster stellar light appears to be dropping at a larger radius.

Moving forward, there are multiple follow-up opportunities from our measurements. For example, in this paper, we have only studied the average properties of galaxy clusters in richness-redshift subsamples using a 'stacking' method. As demonstrated in Golden-Marx et al. (2023a), it is possible to acquire diffuse light measurements of individual galaxy clusters, especially within the 300 kpcs radial range. This would allow us to study how diffuse light properties may change with cluster ellipticity, dynamical state, or with CG properties. It may also be interesting to compare the diffuse light to other galaxy cluster measurements, such as their weak lensing signals as done in Sampaio-Santos et al. (2021).

That said, there are also limitations in this study, especially related to the masking depth as discussed in Section 5. The redshift evolution results reported here are limited by the masking depth of cluster galaxies detected by DES. Faint or undetected cluster galaxies below the masking magnitude limit would have blended into our diffuse light measurements. In this analysis, we use the luminosity function and a test with a deeper magnitude limit to argue that the contribution from those faint galaxies does not affect our redshift evolution conclusions. However, this masking issue can be largely avoided by using a much deeper photometric catalogue to more thoroughly mask the contribution of cluster galaxies. Future cosmic surveys like the Legacy Survey of Space and Time (LSST) from the Vera C. Rubin Observatory will be able to provide such a photometric catalogue.

On a different note, those future surveys will also provide many more photons, and a much larger cluster sample for this 'stacking' (averaging) method, significantly improving the accuracy of diffuse light measurements. Meanwhile, space-based cosmic survey programs like Euclid and the Nancy Grace Roman Telescope can provide imaging data that are less affected by sky background. We look forward to using those data in the coming years.

ACKNOWLEDGEMENTS

This paper is dedicated to the memory of the pioneering Egyptian/American astronomer, Sahar Allam, a woman whose wisdom, bravery, care, sensitivity, and sense of humor have guided and supported us in the past decade and during the most difficult times. We miss you dearly.

Our analyses are performed with a few software packages, including ASTROPY (Astropy Collaboration 2013, 2018, 2022), NUMPY (Harris et al. 2020), SCIPY (Virtanen et al. 2020), and EMCEE (Foreman-Mackey et al. 2013).

The IllustrisTNG simulations were undertaken with compute time awarded by the Gauss Centre for Supercomputing (GCS) under GCS Large-Scale Projects GCS-ILLU and GCS-DWAR on the GCS share of the supercomputer Hazel Hen at the High Performance Computing Center Stuttgart (HLRS), as well as on the machines of the Max Planck Computing and Data Facility (MPCDF) in Garching, Germany.

Funding for the DES Projects has been provided by the U.S. Department of Energy, the U.S. National Science Foundation, the Ministry of Science and Education of Spain, the Science and Technology Facilities Council of the United Kingdom, the Higher Education Funding Council for England, the National Center for Supercomputing Applications at the University of Illinois at Urbana-Champaign, the Kavli Institute of Cosmological Physics at the University of Chicago, the Center for Cosmology and Astro-Particle Physics at the Ohio State University, the Mitchell Institute for Fundamental Physics and Astronomy at Texas A&M University, Financiadora de Estudos e Projetos, Fundação Carlos Chagas Filho de Amparo à Pesquisa do Estado do Rio de Janeiro, Conselho Nacional de Desenvolvimento Científico e Tecnológico and the Ministério da Ciência, Tecnologia e Inovação, the Deutsche Forschungsgemeinschaft and the Collaborating Institutions in the DES.

The Collaborating Institutions are Argonne National Laboratory, the University of California at Santa Cruz, the University of Cambridge, Centro de Investigaciones Energéticas, Medioambientales y Tecnológicas-Madrid, the University of Chicago, University College London, the DES-Brazil Consortium, the University of Edinburgh, the Eidgenössische Technische Hochschule (ETH) Zürich, Fermi National Accelerator Laboratory, the University of Illinois at Urbana-Champaign, the Institut de Ciències de l'Espai (IEEC/CSIC), the Institut de Física d'Altes Energies, Lawrence Berkeley National Laboratory, the Ludwig-Maximilians Universität München and the associated Excellence Cluster Universe, the University of Michigan, NSF's NOIRLab, the University of Nottingham, The Ohio State University, the University of Pennsylvania, the University of Portsmouth, SLAC National Accelerator Laboratory, Stanford University, the University of Sussex, Texas A&M University, and the OzDES Membership Consortium.

Based in part on observations at Cerro Tololo Inter-American Observatory at NSF's NOIRLab (NOIRLab Prop. ID 2012B-0001; PI: J. Frieman), which is managed by the Association of Universities for Research in Astronomy (AURA) under a cooperative agreement with the National Science Foundation.

The DES data management system is supported by the National Science Foundation under Grant Numbers AST-1138766 and AST-1536171. The DES participants from Spanish institutions are partially supported by MICINN under grants ESP2017-89838, PGC2018-094773, PGC2018-102021, SEV-2016-0588, SEV-2016-0597, and MDM-2015-0509, some of which include ERDF funds from the European Union. IFAE is partially funded by the CERCA program of the Generalitat de Catalunya. Research leading to these results has received funding from the European Research Council under the European Union's Seventh Framework Program (FP7/2007-2013) including ERC grant agreements 240672, 291329, and 306478. We acknowledge support from the Brazilian Instituto Nacional de Ciência e Tecnologia (INCT) do e-Universo (CNPq grant 465376/2014-2).

This manuscript has been authored by Fermi Research Alliance, LLC under Contract No. DE-AC02-07CH11359 with the U.S. Department of Energy, Office of Science, Office of High Energy Physics.

DATA AVAILABILITY

The data underlying this article were accessed from the DES and Illustris-TNG database. The derived data generated in this research will be shared on reasonable request to the corresponding author.

REFERENCES

Abbott T. M. C. et al., 2018, ApJS, 239, 18
Abbott T. M. C. et al., 2020, Phys. Rev. D, 102, 023509
Abbott T. M. C. et al., 2021, ApJS, 255, 20

Abbott T. M. C. et al., 2022a, Phys. Rev. D, 105, 023520
Abbott T. M. C. et al., 2022b, Phys. Rev. D, 105, 043512
Abraham R., van Dokkum P., Conroy C., Merritt A., Zhang J., Lokhorst D., Danieli S., Mowla L., 2017, in Knapen J. H., Lee J. C., Gil de Paz A.eds, Astrophysics and Space Science Library Vol. 434, Outskirts of Galaxies. p. 333, preprint (arXiv:1612.06415),
Ahad S. L., Bahé Y. M., Hoekstra H., 2023, MNRAS, 518, 3685
Alonso Asensio I., Dalla Vecchia C., Bahé Y. M., Barnes D. J., Kay S. T., 2020, MNRAS, 494, 1859
Anbajagane D., Evrard A. E., Farahi A., Barnes D. J., Dolag K., McCarthy I. G., Nelson D., Pillepich A., 2020, MNRAS, 495, 686
Arnaboldi M., Gerhard O. E., 2022, FrASS, 9, 403,(arXiv:2212.09569)
Arnaboldi M., Ventimiglia G., Iodice E., Gerhard O., Coccato L., 2012, A&A, 545, A37
Astropy Collaboration, 2013, A&A, 558, A33
Astropy Collaboration, 2018, AJ, 156, 123
Astropy Collaboration, 2022, APJ, 935, 167
Barai P., Brito W., Martel H., 2009, JA&A, 30, 1
Barbosa C. E., Arnaboldi M., Coccato L., Hilker M., Mendes de Oliveira C., Richtler T., 2016, A&A, 589, A139
Barfety C. et al., 2022, ApJ, 930, 25
Behroozi P. S., Wechsler R. H., Conroy C., 2013, ApJ, 770, 57
Bernstein R. A., 2007, ApJ, 666, 663
Bernstein G. M. et al., 2017a, PASP, 129, 074503
Bernstein G. M. et al., 2017b, PASP, 129, 114502
Bernstein G. M. et al., 2018, PASP, 130, 054501
Bertin E., Arnouts S., 1996, A&AS, 117, 393
Bertin E., Mellier Y., Radovich M., Missonnier G., Didelon P., Morin B., 2002, in Bohlender D. A., Durand D., Handley T. H.eds, Astronomical Society of the Pacific Conference Series Vol. 281, Astronomical Data Analysis Software and Systems XI. p. 228
Bleem L. E. et al., 2020, ApJS, 247, 25
Brough S. et al., 2024, MNRAS, 528, 771
Bruzual G., Charlot S., 2003, MNRAS, 344, 1000
Burke C., Collins C. A., Stott J. P., Hilton M., 2012, MNRAS, 425, 2058
Burke D. L. et al., 2018, AJ, 155, 41
Cañas R., Lagos C. d. P., Elahi P. J., Power C., Welker C., Dubois Y., Pichon C., 2020, MNRAS, 494, 4314
Cannarozzo C. et al., 2023, MNRAS, 520, 5651
Chabrier G., 2003, PASP, 115, 763
Chen X., Zu Y., Shao Z., Shan H., 2022, MNRAS, 514, 2692
Chun K., Shin J., Smith R., Ko J., Yoo J., 2023, ApJ, 943, 148
Coccato L., Gerhard O., Arnaboldi M., 2010a, MNRAS, 407, L26
Coccato L., Arnaboldi M., Gerhard O., Freeman K. C., Ventimiglia G., Yasuda N., 2010b, A&A, 519, A95
Coccato L., Gerhard O., Arnaboldi M., Ventimiglia G., 2011, A&A, 533, A138
Conroy C., Wechsler R. H., Kravtsov A. V., 2007, ApJ, 668, 826
Contini E., 2021, Galaxies, 9, 60
Contini E., Gu Q., 2021, ApJ, 915, 106
Contini E., De Lucia G., Villalobos Á., Borgani S., 2014, MNRAS, 437, 3787
Contini E., Yi S. K., Kang X., 2018, MNRAS, 479, 932
Contini E., Yi S. K., Kang X., 2019, ApJ, 871, 24
Contini E., Chen H. Z., Gu Q., 2022, ApJ, 928, 99
Cooper A. P., Gao L., Guo Q., Frenk C. S., Jenkins A., Springel V., White S. D. M., 2015, MNRAS, 451, 2703
Costanzi M. et al., 2019, MNRAS, 482, 490
Cui W. et al., 2014, MNRAS, 437, 816
DES Collaboration, 2005, preprint (arXiv:astro-ph/0510346)
DES Collaboration et al., 2022, PRD, 107, 083504
De Lucia G., Blaizot J., 2007, MNRAS, 375, 2
DeMaio T. N., 2017, PhD thesis, University of Florida
DeMaio T., Gonzalez A. H., Zabludoff A., Zaritsky D., Bradač M., 2015, MNRAS, 448, 1162
DeMaio T., Gonzalez A. H., Zabludoff A., Zaritsky D., Connor T., Donahue M., Mulchaey J. S., 2018, MNRAS, 474, 3009
DeMaio T. et al., 2020, MNRAS, 491, 3751
Diehl H. T. et al., 2018, in Observatory Operations: Strategies, Processes, and Systems VII. p. 107040D, SPIE Peck A.B. Seaman R. Benn C.
Dolag K., Murante G., Borgani S., 2010, MNRAS, 405, 1544
Drlica-Wagner A. et al., 2018, ApJS, 235, 33
Edwards L. O. V., Alpert H. S., Trierweiler I. L., Abraham T., Beizer V. G., 2016, MNRAS, 461, 230
Edwards L. O. V. et al., 2020, MNRAS, 491, 2617
Efron B., 1982, The Jackknife, the Bootstrap and other Resampling Plans. Society for Industrial and Applied MathematicsPhiladelphiaPAUSA
Farahi A. et al., 2019, MNRAS, 490, 3341
Flaugher B. et al., 2015, AJ, 150, 150
Foreman-Mackey D., Hogg D. W., Lang D., Goodman J., 2013, PASP, 125, 306
Furnell K. E. et al., 2021, MNRAS, 502, 2419
Golden-Marx J. B. et al., 2022, ApJ, 928, 28
Golden-Marx J. B. et al., 2023a, MNRAS, 521, 478
Golden-Marx J. B., Zu Y., Wang J., Li H., Zhang J., Yang X., 2023b, MNRAS, 524, 4455
Gonzalez A. H., Zabludoff A. I., Zaritsky D., 2005, ApJ, 618, 195
Gonzalez A. H., Sivanandam S., Zabludoff A. I., Zaritsky D., 2013, ApJ, 778, 14
Gruen D., Bernstein G. M., Jarvis M., Rowe B., Vikram V., Plazas A. A., Seitz S., 2015, J. Instrum., 10, C05032
Gu M. et al., 2020, ApJ, 894, 32
Hansen S. M., Sheldon E. S., Wechsler R. H., Koester B. P., 2009, ApJ, 699, 1333
Harris K. A. et al., 2017, MNRAS, 467, 4501
Harris C. R. et al., 2020, Nature, 585, 357
Hilker M., Richtler T., Barbosa C. E., Arnaboldi M., Coccato L., Mendes de Oliveira C., 2018, A&A, 619, A70
Huang S. et al., 2020, MNRAS, 492, 3685
Huang S. et al., 2022, MNRAS, 515, 4722
Joo H., Jee M. J., 2023, Nature, 613, 37
Kelly P. et al., 2023, preprint (arXiv:2310.13207)
King I. R., 1971, PASP, 83, 199
Kluge M., Bender R., Riffeser A., Goessl C., Hopp U., Schmidt M., Ries C., 2021, ApJS, 252, 27
Krick J. E., Bernstein R. A., 2007, AJ, 134, 466
Krick J. E., Bernstein R. A., Pimbblet K. A., 2006, AJ, 131, 168
Krick J. E., Bridge C., Desai V., Mihos J. C., Murphy E., Rudick C., Surace J., Neill J., 2011, ApJ, 735, 76
Kron R. G., 1980, ApJS, 43, 305
Lan T.-W., Ménard B., Mo H., 2016, MNRAS, 459, 3998
Leung Y. et al., 2020, Res. Notes Am. Astron. Soc., 4, 174
Li R. et al., 2019, MNRAS, 490, 2124
Li J. et al., 2022, MNRAS, 515, 5335
Lidman C. et al., 2012, MNRAS, 427, 550
Lin Y.-T., Brodwin M., Gonzalez A. H., Bode P., Eisenhardt P. R. M., Stanford S. A., Vikhlinin A., 2013, ApJ, 771, 61
Lin S.-C., Su Y., Liang G., Zhang Y., Jacobs N., Zhang Y., 2022, MNRAS, 512, 3885
Longobardi A., Arnaboldi M., Gerhard O., 2015a, Galaxies, 3, 212
Longobardi A., Arnaboldi M., Gerhard O., Hanuschik R., 2015b, A&A, 579, A135
Longobardi A., Arnaboldi M., Gerhard O., Pulsoni C., Söldner-Rembold I., 2018a, A&A, 620, A111
Longobardi A. et al., 2018b, ApJ, 864, 36
Mackie G., 1992, ApJ, 400, 65
Mantz A. B. et al., 2016, MNRAS, 463, 3582
Marinacci F. et al., 2018, MNRAS, 480, 5113
Marini I., Borgani S., Saro A., Murante G., Granato G. L., Ragone-Figueroa C., Taffoni G., 2022, MNRAS, 514, 3082
Martel H., Barai P., Brito W., 2012, ApJ, 757, 48
McClintock T. et al., 2019, MNRAS, 482, 1352
Melchior P. et al., 2017, MNRAS, 469, 4899
Mihos J. C., 2019, preprint (arXiv:1909.09456)
Moffat A. F. J., 1969, A&A, 3, 455
Monaco P., Murante G., Borgani S., Fontanot F., 2006, ApJ, 652, L89

Montes M., 2022, Nature Astron., 6, 308
Montes M., Trujillo I., 2014, ApJ, 794, 137
Montes M., Trujillo I., 2019, MNRAS, 482, 2838
Montes M., Trujillo I., 2022, ApJ, 940, L51
Morganson E. et al., 2018, PASP, 130, 074501
Murante G. et al., 2004, ApJ, 607, L83
Murante G., Giovalli M., Gerhard O., Arnaboldi M., Borgani S., Dolag K., 2007, MNRAS, 377, 2
Murata R., Nishimichi T., Takada M., Miyatake H., Shirasaki M., More S., Takahashi R., Osato K., 2018, ApJ, 854, 120
Naiman J. P. et al., 2018, MNRAS, 477, 1206
Nelson D. et al., 2018, MNRAS, 475, 624
Nelson D. et al., 2019, Comput. Astrophys. Cosmol., 6, 2
Norberg P., Baugh C. M., Gaztañaga E., Croton D. J., 2009, MNRAS, 396, 19
O'Donnell J. H. et al., 2022, ApJS, 259, 1, 27
Oser L., Ostriker J. P., Naab T., Johansson P. H., Burkert A., 2010, ApJ, 725, 2312
Pérez-Hernández E., Kemp S. N., Ramirez-Siordia V. H., Nigoche-Netro A., 2022, MNRAS, 511, 201
Pillepich A. et al., 2018, MNRAS, 475, 648
Plazas A. A., Bernstein G. M., Sheldon E. S., 2014, PASP, 126, 750
Presotto V. et al., 2014, A&A, 565, A126
Puchwein E., Springel V., Sijacki D., Dolag K., 2010, MNRAS, 406, 936
Puddu E. et al., 2021, A&A, 645, A9
Purcell C. W., Bullock J. S., Zentner A. R., 2007, ApJ, 666, 20
Racine R., 1996, PASP, 108, 699
Radovich M. et al., 2020, MNRAS, 498, 4303
Ragusa R. et al., 2023, A&A, 670, L20
Rozo E. et al., 2010, ApJ, 708, 645
Rudick C. S., Mihos J. C., McBride C., 2006, ApJ, 648, 936
Rudick C. S., Mihos J. C., Frey L. H., McBride C. K., 2009, ApJ, 699, 1518
Rudick C. S., Mihos J. C., McBride C. K., 2011, ApJ, 732, 48
Rykoff E. S. et al., 2012, ApJ, 746, 178
Rykoff E. S. et al., 2014, ApJ, 785, 104
Rykoff E. S. et al., 2016, ApJS, 224, 1
Salpeter E. E., 1955, ApJ, 121, 161
Sampaio-Santos H. et al., 2021, MNRAS, 501, 1300
Saro A. et al., 2015, MNRAS, 454, 2305
Sarron F., Martinet N., Durret F., Adami C., 2018, A&A, 613, A67
Sevilla-Noarbe I. et al., 2021, ApJS, 254, 24
Sevilla I. et al., 2011, Proceedings of the DPF-2011 Conference, Providence, RI, August 8-13, 2011 (arXiv:1109.6741)
Shin J., Lee J. C., Hwang H. S., Song H., Ko J., Smith R., Kim J.-W., Yoo J., 2022, ApJ, 934, 43
Sommer-Larsen J., 2006, MNRAS, 369, 958
Spavone M. et al., 2020, A&A, 639, A14
Springel V. et al., 2018, MNRAS, 475, 676
Stott J. P. et al., 2010, ApJ, 718, 23
Tal T., van Dokkum P. G., 2011, ApJ, 731, 89
Tang L., Lin W., Cui W., Kang X., Wang Y., Contini E., Yu Y., 2018, ApJ, 859, 85
Ventimiglia G., Arnaboldi M., Gerhard O., 2011, A&A, 528, A24
Virtanen P. et al., 2020, Nature Methods, 17, 261
Wetzell V. et al., 2022, MNRAS, 514, 4696
Wu H.-Y. et al., 2022, MNRAS, 515, 4471
Yang X., Mo H. J., van den Bosch F. C., 2008, ApJ, 676, 248
Yoo J., Ko J., Kim J.-W., Kim H., 2021, MNRAS, 508, 2634
Zhang Y. et al., 2016, ApJ, 816, 98
Zhang Y. et al., 2019a, MNRAS, 487, 2578
Zhang Y. et al., 2019b, MNRAS, 488, 1
Zhang Y. et al., 2019c, ApJ, 874, 165
Zibetti S., White S. D. M., Brinkmann J., 2004, MNRAS, 347, 556
Zibetti S., White S. D. M., Schneider D. P., Brinkmann J., 2005, MNRAS, 358, 949
Zwicky F., 1951, PASP, 63, 61
Zwicky F., 1952, PASP, 64, 242
van Dokkum P. G. et al., 2010, ApJ, 709, 1018

[1]*NSF National Optical-Infrared Astronomy Research Laboratory, 950 N Cherry Ave, Tucson, AZ 85719, USA*
[2]*Mitchell Institute for Fundamental Physics and Astronomy, 4242 TAMU 576 University Dr, College Station, TX 77845, USA*
[3]*Department of Astronomy, Shanghai Jiao Tong University, Shanghai 200240, China*
[4]*Observatório Nacional, Rua Gal. José Cristino 77, Rio de Janeiro, RJ - 20921-400, Brazil*
[5]*Fermi National Accelerator Laboratory, P. O. Box 500, Batavia, IL 60510, USA*
[6]*Kavli Institute for Particle Astrophysics & Cosmology, P. O. Box 2450, Stanford University, Stanford, CA 94305, USA*
[7]*SLAC National Accelerator Laboratory, Menlo Park, CA 94025, USA*
[8]*Laboratório Interinstitucional de e-Astronomia - LIneA, Rua Gal. José Cristino 77, Rio de Janeiro, RJ - 20921-400, Brazil*
[9]*Institute of Cosmology and Gravitation, University of Portsmouth, Portsmouth, PO1 3FX, UK*
[10]*University Observatory, Faculty of Physics, Ludwig-Maximilians-Universität, Scheinerstr. 1, D-81679 Munich, Germany*
[11]*Department of Physics & Astronomy, University College London, Gower Street, London, WC1E 6BT, UK*
[12]*Instituto de Astrofisica de Canarias, E-38205 La Laguna, Tenerife, Spain*
[13]*Universidad de La Laguna, Dpto. Astrofísica, E-38206 La Laguna, Tenerife, Spain*
[14]*Institut de Física d'Altes Energies (IFAE), The Barcelona Institute of Science and Technology, Campus UAB, E-08193 Bellaterra (Barcelona) Spain*
[15]*Centre for Extragalactic Astronomy, Durham University, South Road, Durham DH1 3LE, UK*
[16]*Jodrell Bank Center for Astrophysics, School of Physics and Astronomy, University of Manchester, Oxford Road, Manchester, M13 9PL, UK*
[17]*University of Nottingham, School of Physics and Astronomy, Nottingham NG7 2RD, UK*
[18]*Astronomy Unit, Department of Physics, University of Trieste, via Tiepolo 11, I-34131 Trieste, Italy*
[19]*INAF-Osservatorio Astronomico di Trieste, via G. B. Tiepolo 11, I-34143 Trieste, Italy*
[20]*Institute for Fundamental Physics of the Universe, Via Beirut 2, I-34014 Trieste, Italy*
[21]*Hamburger Sternwarte, Universität Hamburg, Gojenbergsweg 112, G-21029 Hamburg, Germany*
[22]*School of Mathematics and Physics, University of Queensland, Brisbane, QLD 4072, Australia*
[23]*Department of Physics, IIT Hyderabad, Kandi, Telangana 502285, India*
[24]*Institute of Theoretical Astrophysics, University of Oslo. P.O. Box 1029 Blindern, NO-0315 Oslo, Norway*
[25]*Kavli Institute for Cosmological Physics, University of Chicago, Chicago, IL 60637, USA*
[26]*Center for Astrophysical Surveys, National Center for Supercomputing Applications, 1205 West Clark St., Urbana, IL 61801, USA*
[27]*Department of Astronomy, University of Illinois at Urbana-Champaign, 1002 W. Green Street, Urbana, IL 61801, USA*
[28]*Santa Cruz Institute for Particle Physics, Santa Cruz, CA 95064, USA*
[29]*Center for Cosmology and Astro-Particle Physics, The Ohio State University, Columbus, OH 43210, USA*
[30]*Department of Physics, The Ohio State University, Columbus, OH 43210, USA*
[31]*Center for Astrophysics | Harvard & Smithsonian, 60 Garden Street, Cambridge, MA 02138, USA*
[32]*Australian Astronomical Optics, Macquarie University, North Ryde, NSW 2113, Australia*
[33]*Lowell Observatory, 1400 Mars Hill Rd, Flagstaff, AZ 86001, USA*
[34]*Jet Propulsion Laboratory, California Institute of Technology, 4800 Oak Grove Dr, Pasadena, CA 91109, USA*
[35]*Departamento de Física Matemática, Instituto de Física, Universidade de São Paulo, CP 66318, São Paulo, SP, 05314-970, Brazil*

[36]*Centro de Investigaciones Energéticas, Medioambientales y Tecnológicas (CIEMAT), Madrid, Spain*
[37]*Institució Catalana de Recerca i Estudis Avançats, E-08010 Barcelona, Spain*
[38]*Department of Physics, Carnegie Mellon University, Pittsburgh, Pennsylvania 15312, USA*
[39]*Department of Physics and Astronomy, Pevensey Building, University of Sussex, Brighton, BN1 9QH, UK*
[40]*School of Physics and Astronomy, University of Southampton, Southampton, SO17 1BJ, UK*
[41]*Computer Science and Mathematics Division, Oak Ridge National Laboratory,Oak Ridge, TN 37831, USA*
[42]*Department of Physics, University of Michigan, Ann Arbor, MI 48109, USA*
[43]*Lawrence Berkeley National Laboratory, 1 Cyclotron Road, Berkeley, CA 94720, USA*

This paper has been typeset from a TEX/LATEX file prepared by the author.